A continuous finite element solution of fluid interface propagation for emergence of cavities and geysering

Jorge Molina[*], Pablo Ortiz

University of Granada, Esc. Ing. Caminos, Campus Fuentenueva, 18071 Granada, Spain

Abstract

A finite element method integrated with flux correction techniques is presented for the solution of two nearly incompressible fluids flow with moving interfaces. The procedure incorporates the advection of a phase function to couple fluids motion and the contact discontinuity, and a modified continuity equation preserving mass conservation by considering the parametric definition of density. Limiting bounds comprise information of interface location, improving responses for flows with low density ratio between fluids. A simple conservative postprocessing restores interface resolution by means of an anisotropic streamlined diffusion equation. Strategies to decrease transition thickness between two fluids are examined, using as background the stability of artificial stratified flows and mass error estimation due to density interpolation. To decrease transition thickness, a novel inexpensive nested-grid refinement is proposed. The method is founded in flux-correction principles, ensuring conservation and monotonicity of the variables during dynamical adaptation. Numerical experiments explore the efficacy of the procedure for demanding tests of phase transport and of the equations of motion for interface problems. The main target of this work is to model the genesis and propagation of air cavities in water pipe flows, thus a substantial part of testing focuses on these challenging phenomena. Weakly compressible fluid assumption is essential for proper momentum transfer between phases in the aforementioned dynamics, particularly for bubble rising process. An axisymmetric solution is also developed as an alternative cost-effective choice of the full three-dimensional model for flows in circular ducts.

1. Introduction

Intrusion of large air pockets into ducts is a recurrent physical event in cities' sewer systems during severe storms. Air is introduced or trapped into pipes during drainage and forms big traveling pockets frequently called cavities, either in contact with the atmosphere or sealed with surrounding water and walls. Since the seminal contribution of Benjamin [1], who studied gravity current dynamics by an inverted problem of flow past a cavity in a duct, several authors have investigated intrusion, propagation and impact at street level of air pockets. For instance, in Ref. [2] author examines the effect of weirs across open ends of ducts in the genesis of cavities, and in Ref. [3] author

---

* Corresponding author.
   E-mail addresses: jorgemolina@ugr.es (J. Molina), portiz@ugr.es (P. Ortiz).

reports the effect of conduit slope on cavity shape and celerity. Some layouts of these experiments are illustrated in Figs. 19 and 22. When air pocket finds a vertical tube with still water, the rise of the bubble along the vertical originates the occurrence of geysering [4] (see Fig. 27(e) as illustration). Most relevant works in the subject were conducted by laboratory investigations and by simplified analytical/numerical approximations (e.g. Ref. [5]).

The problem of cavity formation and propagation involves several of the attributes that make fluid interface numerical modeling a demanding subject. Genesis of cavities develops an interface with regions where transition air/water is well defined, along with zones where transition is diffuse. The diffusive character of the latter is often ascribed to a bore emergence and propagation. Besides, presence of a bore at recurrent low supercritical Froude number is accompanied by a very unstable free surface, causing monitoring of cavity seals a difficult task. Water and air determine a very low density ratio ρ_1/ρ_2, ($\rho_1 < \rho_2$). In this situation, oscillations and overshoots in computed velocity field can appear in the neighborhood of interfaces, creating unphysical accelerations of the fluid with lower density [6]. When both fluids are assumed as incompressible, results are satisfactory for cavity formation and propagation. Nevertheless this premise fails to reproduce adequately momentum transfer between phases for the bubble vertical motion, resulting in poor answers for phase and elevation of the geyser.

Two categories of numerical methods are widely recognized in the field of two fluids flows and moving interfaces modeling. First type comprises those methods based on surface tracking, and second type comprises those methods based on surface capturing. The second course of action establishes interface implicitly and two of the most favored procedures in this category are the volume of fluid method (VOF) (e.g. Ref. [7]), and the Level Set method (LS) [8]. Approaches founded on VOF principles preserve mass by construction, while original level set technique presents mass conservation deficiencies. On the other hand, VOF-founded methods have an essential discontinuous representation of the interface. This drawback is circumvented in the primary LS by advecting a signed distance phase function. Moreover, level set method incorporates a reinitialization step to shrink distortions and to update the transported distance function. Literature in the area is profuse. Among recent comprehensive reviews, Ref. [9] puts emphasis on fixed mesh finite element approaches, while Ref. [10] reviews level set and particle level set methods as well as some modern sharp interface procedures.

To improve mass conservation properties in the level set technique, several alternative methods based on hybrid VOF/LS algorithms have been proposed. The conservative level set method (CLS) [11,12] preserves interface thickness, and enhances substantially conservation of the primary LS. Although CLS follows the intrinsic VOF idea, it includes a reinitialization step as a LS procedure, but to reconstruct interface sharpness. In Refs. [13,14] authors introduce more advanced CLS post-transport procedures to reduce interface errors by using the distance level set function to compute interface normals. These advanced reinitialization processes include the solution of two advection and redistancing/reinitialization equations, or a fast marching algorithm to reconstruct the level set field. In Ref. [15] LS is embedded into a VOF formulation in a monolithic form, avoiding any kind of post-processing step; nonetheless the resulting non-linear solution requires an implicit treatment to avert spurious answers on interface.

This paper presents a continuous finite element method to solve the set of equations of motion for two nearly incompressible fluids. To couple the propagation of the contact discontinuity to the fluid dynamics, density and viscosity are defined for weakly compressible fluids in terms of the solution of an advective transport equation for a phase function. Phase function $\phi \in [0, 1]$ essentially agrees with its definition in VOF procedure. To solve the advection equation for the phase function it is decisive a sign-preserving algorithm to avoid unphysical computed values along the interface. The non-oscillatory finite element method (NFEM) [16], founded on principles of flux correction transport techniques [17–19], preserves sign by limiting element flux contributions derived from a high order solution and an independent low order solution. The method is employed to solve transport equation. High order algorithm for the NFEM is the characteristic based scheme incorporating preservation of second order accuracy for transient advective fields [20]. Low order algorithm is a first order upwind FEM, following the idea of selecting a scheme with the (nearly) minimum diffusion to assure positivity. Further, the entire procedure admits of alternative high order methods, written as a sum of low order solution and antidiffusive element contributions [20]. Sign preserving flux correction is also helpful to decrease the oscillatory behavior of dispersive high order continuous finite element methods. Nevertheless resolution of the contact discontinuity after transport step typically needs a postprocessing to maintain its quality [21], as in the aforementioned CLS algorithm. In the CLS method, reinitialization of phase function is accomplished by combining artificial compression and supplementary diffusion in a new non-linear advection diffusion equation (see Eq. (7) in Ref. [12]). To elude solving an additional equation, authors in Ref. [22] modify transport stage to include artificial compression effect and diffusion, while a limiting

process avoids appearance of negative values. This work proposes an explicit integration of a linear advection equation plus a straightforward reinitialization. These simple steps are very competitive with intricate nonlinear monolithic solutions for the phase. Here, an undemanding postprocessing is constructed by solving an anisotropic parabolic equation, following developments in Ref. [23] for incompressible flows. The parabolic equation embraces streamlined diffusivity in the normal direction of interface. The standard Galerkin discretization and an efficient iterative solution of the diffusion equation provide the conservative enhanced phase function. A correction of diffusive fluxes integrated into the iterative solution preserves bounds of the transport solution.

The non-oscillatory finite element method for the solution of the equations of motion has as high order constituent the Characteristic Based Split (CBS) algorithm (see e.g. [24–26]). Again, low order algorithm is a first order upwind FEM, now extended to a system of coupled transport equations [16]. Both solutions are elaborated for weakly incompressible flow conditions. The leading purpose of correction technique in the fluid flow solution is to alleviate spurious velocity jumps across interface. To reduce substantially computational cost of the complete corrected procedure for the dynamics, correction is conducted only for the predictor velocity field in the split process, leading to a single pressure solution. The reduction is particularly useful when incompressible assumption enforces an implicit calculation, while results when reduction is active do not have noticeable differences in comparison with those given by the complete algorithm. However standard limiting procedure does not shrink wiggles efficiently for very low density ratio conditions. Main cause of this deficit is the definition of bounds, blind to the presence of the interface. We incorporate a flux limiting procedure having information of interface location in the establishment of bounds [23]. Integration of these new limits in the present weakly compressible flow algorithm proves to be beneficial for air cavity sealing problems, with very unstable free surfaces and with very low density ratio.

The continuous discretization of the variables, as well as the continuous interpolation of density across interface, give rise to a virtual stratification between phases. Artificial stratification leads to the amplification of high frequency perturbations in problems with Kelvin–Helmholtz instabilities. Besides, these amplifications can be significant for sharp interface resolutions because stratified flows with high gradient transitions are very unstable. We examine stability for stratified flows defined by density and velocity laws resembling numerical artificial distributions (Appendix A). Stabilizing effect of surface tension is well-known in Kelvin–Helmholtz instability for non-stratified flows [27], and attenuation ascribed to surface tension force of high frequency perturbations is recognized in numerical models (see for instance Refs. [28,29]). In the present approach surface tension force follows a continuous model with a finite thickness [30]. Under this virtual stratified flow state, we scrutinize the stabilizing effect of surface tension. The resulting stability condition for artificial stratified flows reveals the relevance of the equivalent surface tension force when transition length diminishes to values such that the model simulates nearly non-stratified flows.

To achieve a stable sharp interface resolution it is desirable a sufficient decrease of transition thickness between fluids. Several courses of action can be adopted to shrink transition length. For instance, by reducing diffusion in reinitialization step, consequential in the growth of wiggles (see discussion in Ref. [12]), or by adjusting the relation between density and phase function (e.g. Ref. [22]). The latter option is consequential in mass conservation. To elucidate the association between density interpolation and conservation, we formulate a mass error bound (Appendix B). The present model does not introduce mass error originated from density interpolation for two incompressible flows; notwithstanding to preserve mass for weakly compressible flows a modified continuity equation is established. Now, the modified continuity equation considers the parametric definition of density. To seek band thickness decrease, keeping the original interpolation of density, we introduce a new dynamical mesh adaptation method. The procedure assures conservation of the variables in the refinement/unrefinement process, and builds a monotone post-processed field with respect to the primary field. To accomplish an inexpensive procedure we propose a nested-grid refinement, able to introduce a priori in the data structure most of the topology information.

Section 2 contains the continuous and numerical formulation of the method. Section 2.1 reports the formulation of the high order method for two weakly compressible flows and for advection of phase function, and Section 2.2 reports the corresponding formulations of the low order scheme. After a basic account of limiting correction principles in Section 2.3, Section 2.4 gives full information about the limiting procedure for the phase function and about the diffusion equation solution for reinitialization. Section 2.5 reports the correcting technique for the two fluids flow solution. Section 2.6 contains the rationale on artificial fluid stratification, strategies to diminish transition thickness and the formulation of the conservative projection for the refinement process.

Section 3 describes numerical experiments. First part focuses on an assessment of the correction method convergence for advection problems and on two stringent tests for the transport stage. To discuss coalescence among

nearby interfaces, first series of experiments consists of four disks advected by a Gaussian vortex distribution. Second test is a sphere in a transient swirling deformation flow [31]. Next, we discuss the experiment of dam break flow with an obstacle [32]. A main target of the model is the accurate simulation of the states in air cavity dynamics; thus Section 3.5 concentrates on intrusion and propagation of cavities, and geysering. The numerical results are compared with laboratory experiments and are studied for three instances: air cavities in horizontal ducts, sealing of cavities in sloping ducts, and bubbles rising along vertical tubes. To scrutinize the rising of air bubbles in saturated vertical circular ducts, an affordable axisymmetric solution has been developed. The axisymmetric formulation is briefly reported in Section 3.5.3. Geysering phenomenon is illustrated and compared with selected frames captured from real footages recorded in the street. Geysering tests were performed by the axisymmetric version and by the full three dimensional model. Final remarks close the paper.

2. Flow and interface numerical solution

The continuous model is the set of equations of motion for two (nearly) incompressible fluids with background densities ρ_1 and ρ_2, $\rho_1 < \rho_2$, and background dynamic viscosities μ_1 and μ_2, respectively. Background values are defined for a reference pressure p_0. System is written as

$$\frac{\partial \rho}{\partial t} + \nabla \cdot (\rho \mathbf{u}) = 0 \ , \tag{1}$$

$$\frac{\partial \mathbf{u}}{\partial t} + \nabla \cdot (\mathbf{u}\mathbf{u}) = -\frac{1}{\rho}\nabla p + \frac{1}{\rho}\nabla \cdot \tau + \mathbf{g} + \mathbf{T} + \mathbf{Q} \ , \tag{2}$$

in Ω, $t \in [t_0, T]$. Here, $\mathbf{u}$ is the velocity field of both fluids, p is the pressure, τ is the viscous stress tensor, $\mathbf{g}$ is the acceleration of gravity, $\mathbf{T}$ is the surface tension, and $\mathbf{Q} = \mathbf{u}(\nabla \cdot \mathbf{u})$. Flows are assumed isothermal and with a small density variation as a consequence of elastic deformation related to pressure change [26]. Hence $\rho \approx \rho(p_0) + \frac{p - p_0}{a^2}$, where $a = \sqrt{\mathcal{K}/\rho}$ is the acoustic wave velocity, and $\mathcal{K}$ is the elastic bulk modulus.

Density and viscosity are parametrically defined by the phase function ϕ,

$$\rho = \rho_1 + (\rho_2 - \rho_1)\phi + \frac{p - p_0}{a_1^2 + (a_2^2 - a_1^2)\phi},$$

$$\mu = \mu_1 + (\mu_2 - \mu_1)\phi \ , \tag{3}$$

where celerity values a_1, a_2, are those corresponding to the reference densities ρ_1 and ρ_2, respectively. Variation of viscosity due to pressure modification is assumed negligible.

Phase function $\phi \in [0, 1]$, establishing the interface between the two fluids as the iso-surface $\phi = 1/2$. Phase function is computed by means of the advective transport equation,

$$\frac{\partial \phi}{\partial t} + \nabla \cdot (\mathbf{u}\phi) = 0 \ \text{ in } \Omega \ , t \in [t_0, T] \ , \tag{4}$$

with boundary conditions

$$\phi = \overline{\phi}(\mathbf{x}, t) \ \text{ on } \Gamma_\phi^- \quad \text{(a)} \ ,$$

$$\phi \mathbf{u} \cdot \mathbf{n}_b = \overline{\mathbf{q}}_\phi(\mathbf{x}, t) \cdot \mathbf{n}_b \ \text{ on } \Gamma_q^- \quad \text{(b)} \ ,$$

$$\Gamma^- = \Gamma_\phi^- \cup \Gamma_q^- \ , \quad \Gamma^- = \{\mathbf{x} \in \Gamma : (\mathbf{u} \cdot \mathbf{n}_b) \leq 0\} \ ,$$

and initial condition

$$\phi(\mathbf{x}, t_0) = \overline{\phi}_0(\mathbf{x}) \ \text{ in } \Omega \ ,$$

where $(\mathbf{x} = (x_l), l = 1, d)$ and d is the number of space dimensions. The domain Ω in $\mathbf{R}^d$ is bounded by $\Gamma = \Gamma^- + \Gamma^+$, and $\overline{\phi}_0$ and $\overline{\mathbf{q}}_\phi$ are known (the latter a vector) functions (from now on overline designates known values). The inflow boundary is denoted by Γ^- while Γ_q^- includes slip condition if suitable, $\Gamma^+ = \{\mathbf{x} \in \Gamma : (\mathbf{u} \cdot \mathbf{n}_b) > 0\}$ is the outflow boundary, $\mathbf{n}_b$ is the outward unit normal to the boundary, and $[t_0, T]$ is the time interval. Boundary and initial conditions for the two fluids flow equations are detailed in the section of numerical experiments.

Numerical solutions of Eqs. (1), (2), and (4) are performed by the non-oscillatory finite element method designated as NFEM. A key idea of the NFEM is to correct a conservative and sign-preserving predictor algorithm (typically with large diffusion error) with anti-diffusive contributions maintaining the properties of the predictor scheme, resembling the original flux correction idea [17]. Corrections are calculated by limiting the difference between the contributions of a high order method (HO), and those of the predictor method (here called low order solution (LO)). Hence complete solution of Eqs. (1), (2), and (4) demands two numerical approximations to perform flux correction limiting process. For the non-oscillatory finite element procedure proposed, high order solution and low order solution are independent. Prior to report details of the correction procedure and of the interface capturing technique, it is necessary to formulate HO and LO methods.

2.1. High order solution

High order solution of Eqs. (1), (2), and (4) is attained by extending the continuous characteristic based split FEM (CBS) (see e.g. [25]), to incorporate preservation of second order accuracy for transient advective field condition (see Appendix A in [20]). A suitable variable splitting completes the CBS method. Galerkin spatial discretization of Eqs. (1) and (2) is stated in terms of the finite element spaces $\mathcal{V}_i^h$, $\mathcal{U}_i^h$, $\mathcal{W}^h$, $\mathcal{P}^h$, $(i = 1, d)$, defined as

$$\mathcal{V}_i^h \subset \mathcal{V}_i = \{v_i \in H^1(\Omega) \mid v_i = 0 \text{ on } \Gamma_q\} \,,$$

$$\mathcal{U}_i^h \subset \mathcal{U}_i = \{u_i \in H^1(\Omega) \mid u_i = \overline{q}_i \text{ on } \Gamma_q\} \,, (i = 1, d) \,,$$

$$\mathcal{W}^h \subset \mathcal{W} = \{w \in H^1(\Omega) \mid w = 0 \text{ on } \Gamma_p\} \,,$$

$$\mathcal{P}^h \subset \mathcal{P} = \{p \in H^1(\Omega) \mid p = \overline{p} \text{ on } \Gamma_p\} \,,$$

where Γ_q is the portion of boundary with prescribed velocity denoted as $\overline{\mathbf{q}}$ and Γ_p specifies the portion of the boundary with prescribed pressure denoted as $\overline{p}$. In particular, this work restricts to linear triangular and tetrahedral finite elements. The method is formulated as: Find $(u_i^h)^{n+1} \in \mathcal{U}_i^h$, $(i = 1, d)$ and $(p^h)^{n+1} \in \mathcal{P}^h$ for all $t \in [t_o, T]$, such that

$$\left(v_i^h, \frac{\Delta u_i^h}{\Delta t}\right)_\Omega = \left(v_i^h, \frac{\Delta u_i^{*h}}{\Delta t}\right)_\Omega - \left(v_i^h, \frac{1}{\rho}(\nabla p^h)_i\right)_\Omega^{n+\theta} \,, (i = 1, d) \tag{5}$$

and

$$\left(\frac{1}{(a^2)^{n+1/2}} w^h, \frac{\Delta p^h}{\Delta t}\right)_\Omega + \frac{\theta \Delta t}{2}\left\langle \nabla w^h, \frac{(\rho')^{n+1/2}}{\rho^{n+1/2}}\nabla(\Delta p^h)\right\rangle_\Omega = -\left(w^h, \nabla \cdot (\rho' \mathbf{u}^h)\right)_\Omega^n + \frac{1}{2}\langle \nabla w^h, (\rho')^{n+1/2}\Delta \mathbf{u}^{*h}\rangle_\Omega$$

$$- \frac{\Delta t}{2}\left\langle \nabla w^h, \frac{\rho'}{\rho}\nabla p^h\right\rangle_\Omega^n - \frac{1}{2}\left[w^h, (\rho')^{n+1/2}\Delta \mathbf{u}^h\right]_\Gamma \,, \quad \forall \, v_i^h \in \mathcal{V}_i^h, \quad w^h \in \mathcal{W}^h \,, \tag{6}$$

where

$$(v, w)_\Omega = \int_\Omega v \, w \, d\Omega \,, \quad \langle \mathbf{v}, \mathbf{w}\rangle_\Omega = \int_\Omega (\mathbf{v} \cdot \mathbf{w}) \, d\Omega \,, \quad [v, \mathbf{c}]_\Gamma = \int_\Gamma v \, \mathbf{c} \cdot \mathbf{n}_b \, d\Gamma \,,$$

$\Delta \mathbf{u}^h = (\mathbf{u}^h)^{n+1}\text{-}(\mathbf{u}^h)^n$, $\Delta p^h = (p^h)^{n+1}\text{-}(p^h)^n$ (superscripts $n+1$ and n indicate time levels t^{n+1} and t^n respectively), $\Delta \mathbf{u}^{*h}$ is a predictor velocity increment, Δt is the time increment, and $\mathbf{c}$ is a vector. Velocity increment $\Delta \mathbf{u}$ has been eliminated in Eq. (6) by replacing the divergence of Eq. (5) (before spatial discretization) into the mass conservation law, a usual practice in velocity correction methodologies; nevertheless velocity increment is kept in last term of Eq. (6) to facilitate the imposition of boundary conditions. The density $\rho' = \rho_1 + \dfrac{p - p_0}{a_1^2 + (a_2^2 - a_1^2)\phi}$, and results from the insertion of parametrical definition of density for nearly incompressible flows (3) into continuity equation. Specific details about this replacement are discussed in Section 2.6. For a variable ψ, time integration parameter θ is defined such that $\psi^{n+\theta} = (1-\theta)\psi^n + \theta \psi^{n+1}$, and superscript $n + 1/2$ signifies $\psi^{n+1/2} = 1/2(\psi^n + \psi^{n+1})$. Mass conservation form is written in agreement with a second order accuracy in time calculation of the predictor velocity increment, specified below (Eq. (7)).

Solution is computed on a sequential basis. First, the predictor velocity increment $\Delta \mathbf{u}^{*h} = \mathbf{u}^{*h} - (\mathbf{u}^h)^n$ is given by

$$
\left(v_i^h, \frac{\Delta u_i^{*h}}{\Delta t} \right)_{\Omega} = - \left(v_i^h, \nabla \cdot \left((\mathbf{u}^h)^{n+1/2} (u_i^h)^n \right) \right)_{\Omega} + \left(v_i^h, f_i^h \right)_{\Omega}^{n+1/2} + \left(v_i^h, g_i \right)_{\Omega}^n
$$

$$
- \frac{\Delta t}{2} \left\{ \left\langle \nabla \cdot \left(v_i^h \left(\mathbf{u}^h \mathbf{u}^h \right)^{n+1/2} \right), \nabla (u_i^h)^n \right\rangle_{\Omega_I} - \left\langle v_i^h \left((\mathbf{u}^h)^{n+1/2} \cdot \nabla (\mathbf{u}^h)^n \right), \nabla (u_i^h)^n \right\rangle_{\Omega_I} \right.
$$

$$
+ \left(\nabla \cdot v_i^h (\mathbf{u}^h)^{n+1/2}, \left(u_i^h \nabla \cdot \mathbf{u}^h \right)^n \right)_{\Omega_I}
$$

$$
\left. + \left(v_i^h, (\mathbf{u}^h)^{n+1/2} \cdot (\nabla (f_i^h + g_i))^n \right)_{\Omega_I} + \left(\nabla \cdot v^h (\mathbf{u}^h)^{n+1/2}, (\nabla p^h)_i^n \right)_{\Omega_I} \right\} , \tag{7}
$$

where $\mathbf{f} = \frac{\mu}{\rho} \nabla^2 \mathbf{u} + \mathbf{T} + \mathbf{Q}$. Under the assumption of nearly incompressible flows, those viscous terms depending on velocity divergence are neglected. Supplemental integration by parts of viscous term (second term on the right hand side of Eq. (7)) is omitted for brevity. Second, pressure is given by Eq. (6). Auxiliary fields used for computation belong to the space of primitive variables and they are not listed for simplicity. The domain Ω is subdivided by E elements Ω_j, $(j = 1, E)$ such that $\Omega = \bigcup \Omega_j$, while Ω_I is the domain without elements with sides belonging to the boundary. Finally, velocity is corrected by means of Eq. (5).

To define the discrete form for the advective transport of phase function ϕ, finite element spaces are $\mathcal{W}^h \subset \mathcal{W} = \{ w \in H^1(\Omega) \mid w = 0 \text{ on } \Gamma_\phi^- \}$ and $\Phi^h \subset \Phi = \{ \phi \in H^1(\Omega) \mid \phi = \overline{\phi} \text{ on } \Gamma_\phi^- \}$. Solution is formulated as: Find $\phi^h \in \Phi^h$ such that

$$
\left(w^h, \frac{\Delta \phi^h}{\Delta t} \right)_{\Omega} = \left(\mathbf{u}^{n+1/2} \cdot \nabla w^h, (\phi^h)^n \right)_{\Omega} - \frac{\Delta t}{2} \left\{ \left\langle \nabla \cdot \left(w^h \left(\mathbf{u}^h \mathbf{u}^h \right)^{n+1/2} \right), \nabla (\phi^h)^n \right\rangle_{\Omega_I} \right.
$$

$$
- \left\langle w^h \left((\mathbf{u}^h)^{n+1/2} \cdot \nabla (\mathbf{u}^h)^n \right), \nabla (\phi^h)^n \right\rangle_{\Omega_I}
$$

$$
\left. + \left(\nabla \cdot w^h (\mathbf{u}^h)^{n+1/2}, \left(\phi^h \nabla \cdot \mathbf{u}^h \right)^n \right)_{\Omega_I} \right\} - \left[w^h, \phi^h \mathbf{u} \right]_{\Gamma^+}^n - \left[w^h, \overline{\mathbf{q}}_\phi \right]_{\Gamma_q^-}^n , \quad \forall \, w^h \in \mathcal{W}^h . \tag{8}
$$

where $\Delta \phi^h = (\phi^h)^{n+1} - (\phi^h)^n$.

To compute velocities at $n + 1/2$, required by Eqs. (7) and (8), we propose a one level second order predictor–corrector procedure. Prior to outline the procedure, Eq. (7) is condensed by introducing the operator $\mathcal{G}$ such that

$$
\left(v_i^h, \frac{\Delta u_i^{*h}}{\Delta t} \right)_{\Omega} = \mathcal{G} \left(\mathbf{u}^{n+1/2}, \mathbf{u}^n, \mathbf{f}^n, \mathbf{g}^n, p^n \right) . \tag{9}
$$

Now, Eqs. (5) and (9) are used to compute a predictor value $\widehat{\mathbf{u}}$ as

$$
\left(v_i^h, \frac{\widehat{\Delta u_i^h}}{\Delta t} \right)_{\Omega} = \mathcal{G} \left(\mathbf{u}^n, \mathbf{u}^n, \mathbf{f}^n, \mathbf{g}^n, p^n \right) - \left(v_i^h, \frac{1}{\rho} (\nabla p^h)_i \right)_{\Omega}^n ,
$$

where values at $n + 1/2$ were assumed as those corresponding at n. Then, values of $\mathbf{u}^{n+1/2}$ in Eq. (9) are calculated as $\mathbf{u}^{n+1/2} = \frac{1}{2} (\mathbf{u}^n + \widehat{\mathbf{u}})$. Computation of $\mathbf{u}^{n+1/2}$ is performed before the phase function advection step, hence intermediate velocity field is ready to be used in Eq. (8) and to be reused in the calculation of the predictor velocity by Eq. (9). Density $\rho^{n+1/2}$ is computed by Eqs. (8) and (3) before proceeding with pressure solution (6); accordingly, celerity $(a^2)^{n+1/2} = a_1^2 + (a_2^2 - a_1^2) \phi^{n+1/2}$ in Eq. (6). To compute ρ', pressure is approximated as $p \approx p^n$.

Surface tension force is calculated following the continuous model with finite thickness formulated in Ref. [30]. Equivalent volume force is

$$
\mathbf{T} = \frac{2\sigma}{\rho_1 + \rho_2} \kappa \frac{\nabla \rho}{(\rho_2 - \rho_1)} , \tag{10}
$$

where σ is the surface tension coefficient and $\kappa = -\nabla \cdot \frac{\nabla \phi}{|\nabla \phi|}$ is the interface curvature. To calculate the curvature, gradient of phase function is recovered at nodes employing improved interface normals attained by the procedure described in Section 2.4. Interface curvature, transition thickness and an interpolation function with bounded support, dependent on the density profile across interface [30], determine the upper bound of surface tension force term.

The bound is independent on densities' jump, hence Eq. (10) is well conditioned, even for flows with two fluids with close values of density.

For stationary velocity fields, $\mathbf{u}^{n+1/2} = \mathbf{u}^n$, and an abridged computation of predictor velocity that eliminates first order truncation errors can be employed,

$$\left(v_i^h, \frac{\Delta u_i^{*h}}{\Delta t}\right)_\Omega = -\left(v_i^h, \nabla \cdot \left(\mathbf{u}^h u_i^h\right) - (f_i^h + g_i)\right)_\Omega^n - \frac{\Delta t}{2}\left(\nabla \cdot \left(v_i^h \mathbf{u}^h\right), \nabla \cdot \left(u_i^h \mathbf{u}^h\right) - (f_i^h + g_i) + (\nabla p^h)_i\right)_{\Omega_I}^n,$$
(11)

while second order solution (8) for transport of phase function results in

$$\left(w^h, \frac{\Delta \phi^h}{\Delta t}\right)_\Omega = \left(\mathbf{u} \cdot \nabla w^h, \phi^h\right)_\Omega^n - \frac{\Delta t}{2}\left(\nabla \cdot (w^h \mathbf{u}), \nabla \cdot (\phi^h \mathbf{u})\right)_{\Omega_I}^n - \left[w^h, \phi^h \mathbf{u}\right]_{\Gamma^+}^n - \left[w, \overline{\mathbf{q}}_\phi\right]_{\Gamma^-}^n.$$
(12)

2.2. Low order solution

Low order algorithm in NFEM is a finite element upwind method. In standard manner, its application to the solution of Eqs. (1), (2), and (4) follows the same steps as the high order method. From now on, notation $\mathcal{LO}()$ indicates the low order operator comprising computation of upwind fluxes. Reader can find a full derivation of the low order operator in Ref. [20], Section 3.3.

Low order method is defined as: Find $(u_i^h)_{LO}^{n+1} \in \mathcal{U}_i^h$, $(i = 1, d)$ and $(p^h)_{LO}^{n+1} \in \mathcal{P}^h$ for all $t \in [t_o, T]$, such that

$$\left(v_{iL}^h, \frac{\Delta u_{iLO}^h}{\Delta t}\right)_\Omega = \left(v_{iL}^h, \frac{\Delta u_{iLO}^{*h}}{\Delta t}\right)_\Omega - \left(v_{iL}^h, \frac{1}{\rho}(\nabla p^h)_{iLO}\right)_\Omega^{n+1/2}, \quad (i = 1, d),$$
(13)

where v_{iL}^h corresponds to the lumped mass matrix and LO subindex signifies low order solution. Low order intermediate velocity increment is calculated as

$$\left(v_{iL}^h, \frac{\Delta u_{iLO}^{*h}}{\Delta t}\right)_\Omega = \left(v_i^h, f_i^h\right)_\Omega^n + \left(v_i^h, g_i\right)_\Omega^n + \mathcal{LO}\left((\mathbf{u}^h + \frac{\Delta t}{2}(\mathbf{f}^h + \mathbf{g}))^n, (\mathbf{u}^h)^n\right).$$
(14)

Pressure solution is nearly identical to high order formulation (Eq. (6)) and is not reproduced for brevity. Finally, the discrete low order form for phase function transport is formulated as: Find ϕ_{LO}^h such that

$$\left(w_L^h, \frac{\Delta \phi_{LO}^h}{\Delta t}\right)_\Omega = \mathcal{LO}\left((\phi^h)^n, (\mathbf{u}^h)^n\right),$$
(15)

where w_L^h corresponds to lumped mass matrix. We apply the low order upwind method in an edge-based manner for efficiency [20]. Full low order solution (13) is circumvented by an abridged version with only one computation of the pressure solution. This option is reported in Section 2.5, after the introduction of basics on limiting correction.

2.3. A brief on limiting fluxes by correction

We construct a high order corrected solution $\tilde{\mathbf{B}}_i$ at node i of the finite element mesh $\Omega = \bigcup \Omega_j$, $(j = 1, E)$, and at time $(n+1)\Delta t$ as

$$\tilde{\mathbf{B}}_i^{n+1} = \mathbf{b}_i^{n+1} + \sum_{j=1}^e \tilde{\mathbf{A}}_j = \mathbf{b}_i^{n+1} + \sum_{j=1}^e \mathbf{c}_j \mathbf{A}_j = \mathbf{b}_i^{n+1} + \sum_{j=1}^e \mathbf{c}_j (\mathbf{A}_{HO} - \mathbf{A}_{LO})_j.$$
(16)

High order corrected solution results from updating the low order solution $\mathbf{b}$ at time $(n + 1)\Delta t$ by the sum of corrected antidiffusive element contributions denoted as $\tilde{\mathbf{A}}$. In Eq. (16), $\tilde{\mathbf{A}}_j$ is the corrected anti-diffusive contribution of element j, while $\mathbf{A}_j$ is the difference between the contribution of the high order scheme $\mathbf{A}_{HO}$ and the contribution of the low order scheme $\mathbf{A}_{LO}$ corresponding to element j. Sum extends over e, the number of elements j surrounding node i; summation convention is not used. To compute the anti-diffusive corrections it is necessary to define the elementwise correcting functions $\mathbf{c}_j$'s. The correcting functions depend on nodal high order solution, on nodal low order solution, and on the element contribution to the node of the m variables of the problem. Range of $\mathbf{c}_j$'s is: $0 \leq c_{jm} \leq 1$, $c_{jm} \in \mathbf{c}_j$, $(m = 1, d + 1)$ for Eqs. (1) and (2), and $m = 1$ for Eq. (4). For $c_{jm} = 1$ the corrected

solution equals the high order solution; for $c_{jm} = 0$ solution equals the low order solution. Reader can refer to Ref. [16] for a thorough description of the non-oscillatory corrected procedure.

To impose the positivity of the corrected solution, we introduce at node i the bounds B_i^{min}, B_i^{max} (here written for a scalar equation to simplify). Thus if $B_i^{min} \leq \tilde{B}_i^{n+1} \leq B_i^{max}$, then $\tilde{B}_i^{n+1} \geq 0$. To specify B_i^{min} and B_i^{max}, bounds given by Zalesak are a suitable choice (see equations (17') and (18') in Ref. [33]),

$$B_i^{min} = \min_{j=1,e} \left(B_i^n, b_i^{n+1}, B_k^n, b_k^{n+1} \right), \quad \forall \text{ (nodes } k \neq i) \in j \quad , \tag{17}$$

$$B_i^{max} = \max_{j=1,e} \left(B_i^n, b_i^{n+1}, B_k^n, b_k^{n+1} \right), \quad \forall \text{ (nodes } k \neq i) \in j \quad , \tag{18}$$

where all variables in Eqs. (17) and (18) are positive definite.

Direct extension of scalar correction ($m = 1$) for the complete set of equations of motion ($m = 1, d+1$) could result in inappropriate constraints on some of the variables (see discussions in Refs. [18,34]). Besides, proper synchronization of antidiffusion is relevant to shrink oscillations in the vicinity of the contact discontinuity, in particular for small values of density ratio ρ_1/ρ_2. This work substantiates the action only on velocity components [18] as an effective approach to coordinate corrections. Hence correcting functions for a node i are defined as $c_i = \min(c_{im})$, where m ($m = 1, d$) indicates the velocity component. Correcting functions in Eq. (16) are established by element; for element j the corresponding c_j is $c_j = \min(c_i)$, $\forall$ nodes $i \in j$.

2.4. Limiting fluxes for phase function transport and reinitialization

Limiting process defined by Eq. (16) for phase function, $B = \phi$, acts once high order solution (8) and low order solution (15) of phase function advection equation (4) are attained. Corrected solution for a node i is computed as

$$\tilde{\Phi}_i^{n+1} = (\phi_{LO})_i^{n+1} + \sum_{j=1}^{e} \frac{1}{2} \left[c_c^+ c_j^+ (A_j + |A_j|) + c_c^- c_j^- (A_j - |A_j|) \right], \tag{19}$$

where $\tilde{\Phi}$ is the improved sign-preserving high order phase function solution. The element coefficients c_j are written in terms of four correcting functions, $c_j^+, c_j^-, c_c^+, c_c^-$. Determination of c_j^+ and c_j^- is detailed in Ref. [20], Appendix B. The global coefficients c_c^+ and c_c^- eliminate any high order mass residual due to the limiting procedure, and preserve bounds established by Eqs. (17) and (18). Details of computation of these coefficients as well as a comprehensive examination of high order mass residuals in the NFEM can be found in Ref. [23].

Reinitialization step maintains resolution of the contact discontinuity [21], and adds a reduced amount of diffusion to avoid wiggles on the interface. Standard reinitialization of phase function combines artificial compression and diffusion in a non-linear advection diffusion equation (see e.g. [12]). Here, a non-linear anisotropic diffusion equation merges both effects into the anisotropic diffusivity $\mathcal{D}(\hat{\phi})$. Reconstruction is formulated as: Find $\hat{\phi}^h \in \Phi^h$ such that

$$\left(w_L^h, \frac{\Delta \hat{\phi}^h}{\Delta \tau} \right)_\Omega = -\left(\frac{\partial w^h}{\partial \mathbf{n}}, \mathcal{D}(\hat{\phi}) \frac{\partial \hat{\phi}^h}{\partial \mathbf{n}} \right)_\Omega^m + \left[w^h, \mathcal{D}(\hat{\phi}) \frac{\partial \hat{\phi}^h}{\partial \mathbf{n}} \mathbf{n} \right]_\Gamma^m, \tag{20}$$

where w_L^h corresponds to the lumped mass matrix, τ is a dummy time, $\hat{\phi}$ is the reconstructed phase function, $\mathbf{n} = \frac{\nabla \phi}{|\nabla \phi|}$ is the interface normal, and $\mathcal{D}(\hat{\phi}) \lesseqgtr 0$. In Eq. (20) diffusion is streamlined in the normal direction of the interface. Initial condition is

$$\hat{\phi}(\mathbf{x}, \tau = 0) = \phi(\mathbf{x}, t^{n+1}) . \tag{21}$$

On the boundary we assume natural boundary condition and $\mathbf{n} \cdot \mathbf{n}_b = 0$. The diffusivity coefficient $\mathcal{D}(\hat{\phi}) = \varepsilon \cdot \mathcal{D}_a(\hat{\phi})$, where ε depends on interface thickness and $\mathcal{D}_a(\hat{\phi}) = \hat{\phi} \left(1 - \hat{\phi} \right) / (\frac{\partial \hat{\phi}}{\partial \mathbf{n}} + \varsigma)$, where ς is a small number to avoid the vanishing of the denominator. Coefficient $\mathcal{D}_a(\hat{\phi})$ replaces artificial compression by anti-diffusive action. Lumped mass matrix is applied for dummy time integration (superscript m indicates dummy time level τ^m). Although resulting scheme (20) is conditionally stable, choice of initial condition (21) provides a very fast convergence for the pseudo-time solution stated below. However, given that $\mathcal{D}(\hat{\phi}) \lesseqgtr 0$, positivity of solution is not preserved.

To bound the reconstructed solution by the limits Φ_i^{min} and Φ_i^{max} of transport step, we integrate an ad-hoc correction of diffusive element contributions with the pseudo-time iteration as

$$\hat{\phi}_i^{m+1} = \hat{\phi}_i^m + \sum_{j=1}^{e} c_j A_j^m , \quad c_j = \min\left(c_k^+, c_k^-\right) \ \forall \ \text{nodes} \ k \in j ,$$

where $\hat{\phi}_i^{m+1}$ is the enhanced solution at pseudo-time $(m+1)\Delta\tau$. The correcting functions c_j are computed in terms of bounds defined by solution at $m\Delta\tau$. Complete derivation of new bounds is formulated in Ref. [23].

Computation of interface normals far from interface can produce indeterminacy due to nearly constant values of phase function. To alleviate these spurious values, calculation of interface normal only involves few elements surrounding $\phi = \frac{1}{2}$ contour [23]. Numerical experiments have shown that three layers of elements neighboring the interface are sufficient to a proper capture of the interface.

2.5. Limiting fluxes for two fluids flow solution

To solve the set of equations of fluid flow, the method stated in Section 2.3 requires, in the incompressible limit, the implicit solution of Eq. (6) and the implicit solution of the pressure equation of the low order procedure. Both calculations must be completed each time step to build in the upcoming correction. A cost effective way to circumvent this double computation is by performing correction only for the predictor velocity field. All series of experiments have shown that use of this reduced method instead of the monolithic NFEM has not noticeable differences in results, and the algorithm retains the capability to preserve interface resolution. For simulations as those shown in Section 3.5.2, the extra computational cost of the abridged NFEM with respect to the complete procedure without corrections is about 1% for incompressible fluids (serial computation). In the weakly compressible case, the extra is about 5%, since pressure solver demands a lesser number of iterations to convergence.

The limiting procedure discussed in preceding sections is not able to take action to control artificial velocity jumps across the interface because customary bounds do not identify the presence of the interface. An assessment to distinguish interface location [23] is integrated into the limiting procedure and has the following steps. First, for each node i we identify nodes q surrounding i such that,

$$\left| \phi_i^{n+1} - \phi_q^{n+1} \right| < \Upsilon ,$$

where $\Upsilon = \Upsilon(\delta, \varepsilon)$, and δ is an average element size length. Adequate choice of parameter Υ prevents creation of new limits across the interface (see details in numerical tests). Second, by calling p the total number of q nodes, and considering the reduced method, bounds for k velocity component at node i are computed according to,

If $p > 0$,

$$u_{ik}^{max} = \max_{q=1,p} \left(u_{ik}^n, (u_{LO}^*)_{ik}, u_{qk}^n, (u_{LO}^*)_{qk} \right) , \tag{22}$$

$$u_{ik}^{min} = \min_{q=1,p} \left(u_{ik}^n, (u_{LO}^*)_{ik}, u_{qk}^n, (u_{LO}^*)_{qk} \right) .$$

Else if $p = 0$,

$$u_{ik}^{max} = \max \left(u_{ik}^n, (u_{LO}^*)_{ik} \right) , \tag{23}$$

$$u_{ik}^{min} = \min \left(u_{ik}^n, (u_{LO}^*)_{ik} \right) .$$

Extension of bounds calculation to the unabridged method is straightforward and is not reported for brevity.

2.6. Artificial fluid stratification

Several interface problems, such as air cavity intrusion in ducts, often involve two non-stratified fluids flow, identified by a lower fluid advancing in a specified direction, and an upper lighter fluid moving in the opposite way. Instability of this kind of motion is the widely known Kelvin–Helmholtz instability for non-stratified flows. By assuming a horizontal interface surface and taking into account surface tension, the stability condition [27] is

$$g\left(\rho_2^2 - \rho_1^2\right) + K^2\sigma(\rho_2 + \rho_1) > K\rho_1\rho_2\left(u_2 - u_1\right)^2 , \tag{24}$$

where $K = 2\pi/\lambda$ is the perturbation wave number, λ is the perturbation wavelength, and u_1, u_2 are the tangential velocity for upper fluid and lower fluid, respectively. Eq. (24) shows the apparent stabilizing effect of surface tension for non-stratified flows.

However, numerical model gives rise to a virtual stratification between both phases, ascribable to the parametrical definition of density (3) and to the continuous finite element discretization of the variables. To study effects of this virtual stratification, we perform a stability analysis assuming a sound density distribution across the interface,

$$\rho(y) = \begin{cases} \rho_1 + \frac{\rho_2 - \rho_1}{2} e^{-y/L_\rho} & if \quad y > 0 \\[2mm] \rho_2 + \frac{\rho_1 - \rho_2}{2} e^{y/L_\rho} & if \quad y < 0 \end{cases}, \tag{25}$$

where interface is located at $y = 0$. This constant plus exponential density profile, proposed in Ref. [35] for Rayleigh–Taylor instabilities, is reasonable since density is defined in terms of the phase function, and phase function is the numerical solution of the parabolic equation (20). We consider the same transition thickness for velocity, along the lines of Ref. [36]. Then,

$$u(y) = \begin{cases} u_1 + \frac{u_2 - u_1}{2} e^{-y/L_u} & if \quad y > 0 \\[2mm] u_2 + \frac{u_1 - u_2}{2} e^{y/L_u} & if \quad y < 0 \end{cases}. \tag{26}$$

In these profiles, L_ρ, L_u are parameters that control density and velocity gradient, respectively. Here, one parameter is used, $L_I = L_\rho = L_u$. In the numerical approximation, surface tension force is the volume force with finite thickness established by Eq. (10).

Appendix A reports the formulation of stability conditions for a two phase flow with a diffused interface specified by the density and velocity distributions given by Eqs. (25) and (26), respectively, along with the equivalent surface tension force (10). Solution is achieved by integrating the two dimensional linearized equations governing the perturbation field, and by adopting solutions of the form $\exp(iKx + st)$, where $s \in \mathbb{C}$ and $\mathrm{Re}(s)$ is the perturbation growth rate. The set of equations is reduced to one equation in terms of perturbed vertical velocity $\tilde{v}$,

$$(s + iKu)(K^2 \rho \tilde{v}) - \frac{K^2 g}{s + iKu} \frac{\partial \rho}{\partial y} \tilde{v} + K^4 \sigma \frac{\tilde{v}}{s + iKu} \frac{\partial \rho}{\partial y} \frac{1}{(\rho_1 - \rho_2)} \frac{2\rho}{(\rho_1 + \rho_2)} = 0. \tag{27}$$

Integration of Eq. (27) along vertical direction gives solution (49) (Appendix A).

To illustrate and to discuss results established by Eq. (49) we consider a duct of height d, where water takes up the lower half, and air the upper half. The adequacy of this problem to the unbounded solution is substantiated if chosen values of L_I are such that transition thickness δ_I is a small fraction of d; here, we consider an upper limit δ_I of $0.2d$. Velocities are $u_1 = -1/2\sqrt{gd}$, $u_2 = 1/2\sqrt{gd}$, and $\rho_1/\rho_2 = 0.001$. Fig. 1 depicts the non-dimensional growth rate $\mathrm{Re}(s)\sqrt{d/g}$ as a function of non-dimensional transition thickness δ_I/d, for perturbation wavelengths values of $\lambda/d = 0.25, 0.1, 0.05, 0.025$. Transition thickness $\delta_I = |y_1 - y_2|$, where $\rho(y_1) = 0.99\rho_1 + 0.01\rho_2$ and $\rho(y_2) = 0.01\rho_1 + 0.99\rho_2$; thus $\delta_I = 7.824L_I$. Growth rate is plotted for inviscid cases as solid lines when $\sigma = 0$, and as dashed lines when non-dimensional surface tension coefficient $2\sigma/((\rho_1 + \rho_2)gd^2) = 1.426\cdot10^{-3}$.

First, we examine cases without the action of the equivalent surface tension. Non-stratified flows are stable for perturbations with wavelengths $\lambda/d > 0.0063$ (Eq. (24)). When stratification is active, flows with high gradient transitions are very unstable, particularly in case of short wavelength perturbations. Amplification diminishes for lower gradient transitions because of the stabilizing effect of velocity gradient, in opposition to the destabilizing effect of the density gradient (see e.g. [36]). For sufficiently large values of δ_I, growth rate tends to zero. Now, consider the action of continuous surface tension. Its stabilizing impact is present for all transitions thickness, and it is greater for short wavelength perturbations. For example, case corresponding to $\lambda/d = 0.025$ is not distinguishable in Fig. 1 because flow is stable for all values of transition thickness, and the same occurs for shorter wavelengths. Amplification is discernible if $\delta_I/d \gtrsim 0.03$ and $\lambda/d \geq 0.025$.

When transition length tends to zero, surface tension term tends to its standard representation, and Eq. (27) turns into

$$(s + iKu)(K^2 \rho \tilde{v}) - \frac{K^2 g}{s + iKu} \frac{\partial \rho}{\partial y} \tilde{v} + K^4 \sigma \frac{\tilde{v}}{s + iKu} \delta_d(y) = 0, \tag{28}$$

where δ_d is the Dirac-delta function. In this situation, stability is governed by condition (51) (Appendix A). Fig. 2 shows results for this asymptotic state. In comparison with previous answers, a reduction of amplification rate is
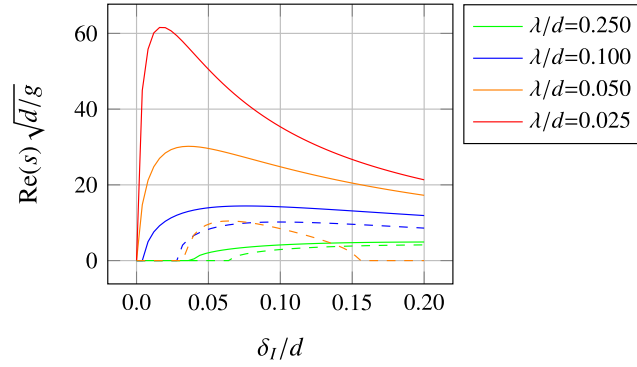
Fig. 1. Non-dimensional growth rate $\text{Re}(s)\sqrt{d/g}$ as a function of non-dimensional transition thickness δ_I/d. Solid and dashed lines are results without and with surface tension, respectively. (For interpretation of the references to color in this figure legend, the reader is referred to the web version of this article.)
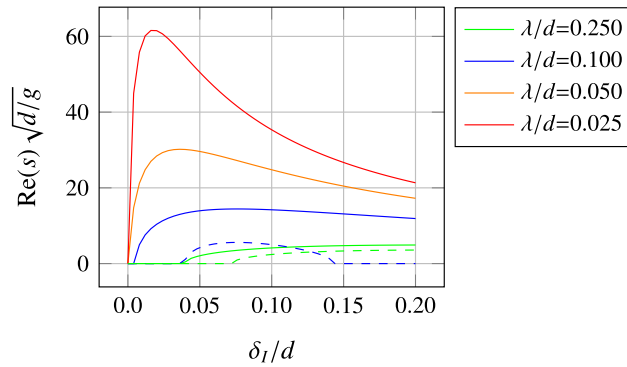

Fig. 2. Non-dimensional growth rate $\text{Re}(s)\sqrt{d/g}$ as a function of non-dimensional transition thickness δ_I/d for the asymptotic case: $\lim_{L_I} \to 0$. Solid and dashed lines are results without and with surface tension, respectively. (For interpretation of the references to color in this figure legend, the reader is referred to the web version of this article.)

observed for all wavelengths. Also, Fig. 2 indicates an increase on the threshold value of δ_I/d whereupon growth rate starts to be perceivable (for higher wavelengths). Notwithstanding the overall response is almost identical to the continuous representation of surface tension.

A sufficient decrease of transition length avoids Kelvin–Helmholtz instabilities for all perturbation wavelengths if surface tension is present (apparent in Figs. 1 and 2). On the opposite side, the stabilizing effect coming from increasing δ_I needs large values of thickness to be effective, enough to deteriorate significantly interface resolution. Some available strategies to decrease thickness can be appraised. Most direct technique is to reduce the diffusivity coefficient ε employed in reinitialization (Eq. (20), where $\mathcal{D}(\hat{\phi}) = \varepsilon \cdot \mathcal{D}_a(\hat{\phi})$). Although a decrease of diffusion coefficient ε on interface improves resolution of the contact discontinuity, too small values of ε originate wiggles in phase function [12].

A different course of action is to adjust original relation between density and phase function (3). In this case, modifications can have consequences in mass conservation. To scrutinize this option, we consider for brevity the incompressible limit and one alternative function to reduce band thickness. In the present model, density becomes a linear interpolation of phase function, $\rho(\phi) = \rho_1(1 - \phi) + \rho_2\phi$. Then mass error is of round-off order if phase function is advected using a conservative method. As alternative function we examine the following interpolation proposed in Ref. [22],

$$\rho(\phi) = \begin{cases} \rho_1 & if & \phi < 1/2 - \vartheta \\ \rho_1 + (\phi - 1/2 + \vartheta)\frac{\rho_2 - \rho_1}{2\vartheta} & if & 1/2 - \vartheta \leq \phi \leq 1/2 + \vartheta \\ \rho_2 & if & \phi > 1/2 + \vartheta\ , \end{cases} \tag{29}$$

where $\vartheta \leq 1/2$ controls the transition gradient. If $\vartheta = 1/2$, present original interpolation is recovered, while for $\vartheta = 0$ interpolation transforms into the Heaviside function. We estimate a bound of mass error $e(M)$ (see Appendix B), along the lines of estimation procedure introduced in Ref. [12], resulting in Eq. (52),

$$|e(M)| < \left| L_\Gamma (\rho_2 - \rho_1)\varepsilon \left(\log\left(\frac{2}{1 + 2\vartheta} \right) + \frac{2\vartheta - 1}{4\vartheta} \log\left((1 + 2\vartheta)(1 - 2\vartheta) \right) \right) \right|.$$

Error bound is proportional to interface length L_Γ and reinitialization parameter ε. Maximum value is $|e(M)|_{\vartheta=0} < |L_\Gamma(\rho_2 - \rho_1)\varepsilon \log(2)|$ for the Heaviside function, in agreement with Ref. [12] without considering $\mathcal{O}(\varepsilon^2)$ terms. For the present model $e(M)_{\vartheta=1/2} = 0$.

For nearly incompressible flows, last term of Eq. (3) is active, and mass conservation is not longer preserved without a proper modification of the continuity equation. Then, to recover mass conservation equation (6) integrates the complete parametrical definition of density into the pressure solution of the high order method. This step must be reproduced for the low order pressure solution if monolithic algorithm is selected.

2.6.1. Mesh refinement

To diminish band thickness we propose an adaptive mesh refinement method. The method preserves the original density interpolation and is conservative for phase, mass, velocity and pressure. Also, new fields are monotone with respect to the original fields. To adapt the mesh to the demands of a moving interface problem the procedure needs, as expected, a dynamic refinement to reduce band thickness and an unrefinement to recover primitive mesh topology. To formulate the procedure, consider a scalar field B. Conservation of a scalar field B in refinement and unrefinement processes [37] is stated in terms of the finite element spaces $V^h \subset V = \{v \in H^1(\Omega)\}$ and $W^h \subset W = \{w \in H^1(\Omega)\}$, where first space is set in the mesh after refinement (unrefinement), and the second space is set in the original mesh. Now, the method is defined as: Find a modified field $B_\dagger^h \in V^h$ such that

$$\left(v^h, B_\dagger^h \right)_\Omega = \left(v^h, B^h \right)_\Omega , \tag{30}$$

where $B^h \in W^h$ is the initial scalar field.

To preserve bounds of original field we employ a form of the correction procedure. The form resembles a conservative and monotone method of projection proposed in Ref. [38] to project pressure field from a fluid domain to a solid domain. Here, low order solution b is determined by premultiplying the right hand side of Eq. (30) by the inverse of the lumped mass matrix of new mesh. Thus low order solution keeps the original bounds. Reconstructed field $\tilde{B}_i$ at node i of new mesh is

$$\tilde{B}_i = b_i + \sum_{j=1}^{e} c_j A_j = b_i + \sum_{j=1}^{e} (\mathbf{M}_L)^{-1} c_j \left\{ (\mathbf{M}_L - \mathbf{M}_C) B_\dagger \right\}_j \tag{31}$$

where e is the number of elements j surrounding node i, c_j's are the elementwise correcting functions detailed in Sections 2.3 and 2.4, A_j is the anti-diffusive flux for element j, $\mathbf{M}_L$ is the lumped mass matrix, and $\mathbf{M}_C$ is the consistent mass matrix. Each definition applies to the new (refined/unrefined) mesh. To calculate nodal bounds, we employ Eqs. (17) and (18), but only including the primitive field B in the original mesh.

Candidates for refinement are the elements contained in a specified number of layers neighboring those elements containing $\phi = 1/2$ value (usually three layers are sufficient[1]). Refinement procedure is performed by nested grids involving mainly static data. Then, topology information can be largely integrated a priori into the data structure, enabling a straightforward dynamic computation. Two options of nested grids were inspected. First option is the division sketched in Fig. 3(a). In this situation, the modified field after refinement is calculated straightforwardly, and procedure described above is only necessary for unrefinement stage. Second option is the division sketched in Fig. 3(b), by adding middle edge nodes. Here, both refinement and unrefinement need the conservative projection. The two alternative procedures give similar results. On one side, first option is cheaper, to a limited extent. On the other side, second option sometimes yields to more regular meshes in the vicinity of the current interface. Adaptive meshing is fulfilled after complete flow and phase computation, and conservative projection is applied to phase function, pressure and velocity field. The burden of refinement/unrefinement procedure is dependent on the interface length and dynamics. As standard examples, simulations in Section 3.5.2 were accomplished by updating the mesh every two time steps on average, and the extra cost value is of around 30% with respect to the experiments with same grid and without adaptivity reported in Section 3.5.1.

---

[1] Maximum value of ε in numerical experiments is $\varepsilon \approx 0.83\delta$. Interface thickness $\eta \approx 6\varepsilon$ (Ref. [12], pp 796), thus $\eta \approx 5\delta$.
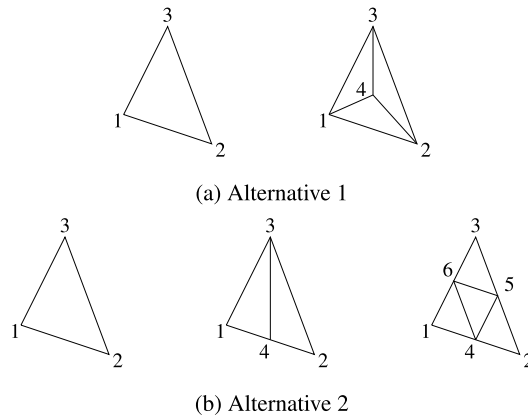
(a) Alternative 1

(b) Alternative 2

Fig. 3. Refinement options.

3. Numerical experiments

3.1. Advection of a Gaussian profile. An assessment of convergence

Prior to experiments on interface dynamics, we include a test to assess the convergence of NFEM for advection problems, comprising precise information on the recovery of second order accuracy once corrections are active, by comparing approximate rates of convergence. Each experiment is performed with nearly constant CFL number and with uniform advection velocity. A Gaussian cone of height 4 is placed at initial time with its center at (-2,-2) of a domain [-50,50]×[-50,50] by prescribing the initial condition as

$$\overline{\phi}_0(\mathbf{x}) = 4 \exp\left(-\frac{1}{2}\left\{\left(\frac{(x+2)}{2}\right)^2 + \left(\frac{(y+2)}{2}\right)^2\right\}\right)$$

where scalar function is denoted as the phase function, and $\mathbf{u} = (2.4, 2.4)$. We generated four unstructured meshes with average element side length[2] $\overline{\delta}$ values of 0.221, 0.44, 0.89, 1.81; comprising 367616, 91636, 22764, 5606 linear triangular elements, and 184613, 46223, 11587, 2908 nodes, respectively. CFL = 0.9 and 0.5 are specified for all meshes, while final time of the experiment corresponds to 16, 8, 4 and $2\Delta t$ for the four grids, respectively.

The solution was calculated by the high order FEM method (Eq. (8)) and by the NFEM. The L_1 and L_2 errors were computed for the HO-FEM and for the NFEM for each mesh and for each CFL, to observe recovery of accuracy once the correction operates. Figs. 4 and 5 depict errors in terms of average element size for CFL = 0.9 and 0.5 respectively. Second order accuracy of the HO-FEM is approximately preserved by NFEM for all the range of CFL numbers. HO-FEM and NFEM methods are always over second order rate, except for values measured in the two coarsest meshes for CFL = 0.9. For this condition, the NFEM has $p \approx 1.95$ while the HO-FEM has $p \approx 2.06$ (errors in L_2 norm). Similar rates of convergence were obtained by doubling the final time of the experiments.

3.2. Gaussian vortex test

We discuss interaction and coalescence among adjacent interfaces by means of a demanding distribution of a scalar function transported by a time dependent Gaussian vortex flow. The test is defined by four disks of radius 15 and height 1, centered at (-25,0), (25,0), (0,-25) and (0,25), respectively, in a $[-50, 50] \times [-50, 50]$ region (see sketch in Fig. 6). The advective velocity field has the following Cartesian components:

$$u(\mathbf{x}, t) = -1747 \frac{y}{r^2} \cdot \left(1 - e^{-\frac{r^2}{\beta^2}}\right) \cdot \cos\left(\frac{\pi t}{T}\right)$$

$$v(\mathbf{x}, t) = 1747 \frac{x}{r^2} \cdot \left(1 - e^{-\frac{r^2}{\beta^2}}\right) \cdot \cos\left(\frac{\pi t}{T}\right)$$

---

[2] Average element side length for unstructured meshes is defined as $\overline{\delta} = \frac{1}{E} \sum_{j=1}^{E} \sqrt{(\Delta x)_j^2 + (\Delta y)_j^2}$.
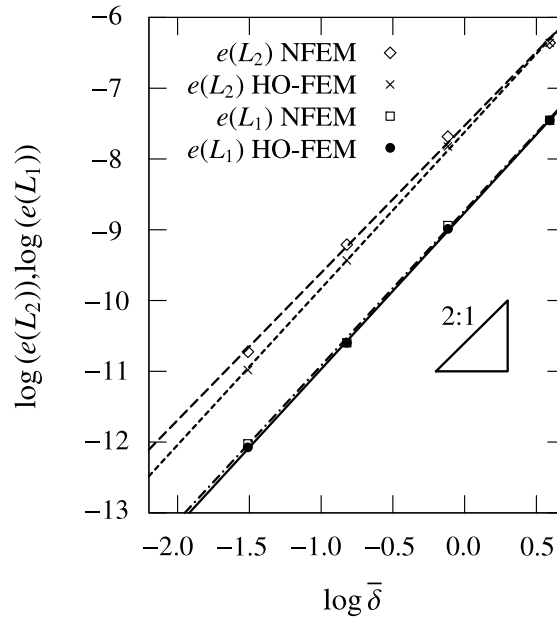
Fig. 4. Gaussian cone test. Convergence for 4 unstructured meshes and CFL≈ 0.9. $e(L_1)$: L_1 error, $e(L_2)$: L_2 error. NFEM: new method. HO-FEM: Characteristic based FEM.
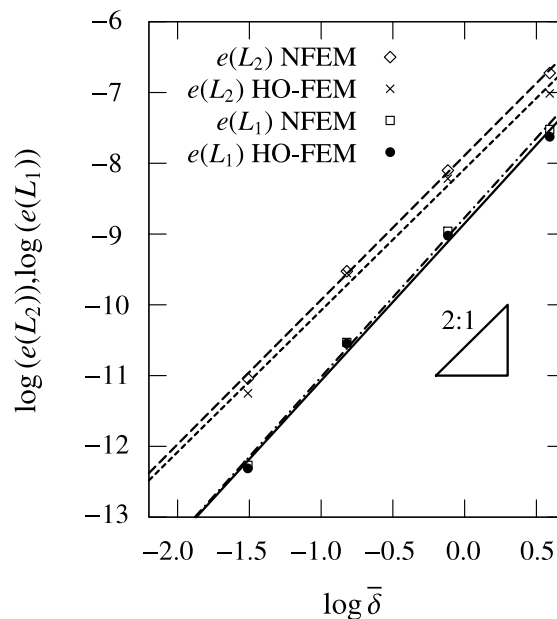

Fig. 5. Gaussian cone test. Convergence for 4 unstructured meshes and CFL≈ 0.5. $e(L_1)$: L_1 error, $e(L_2)$: L_2 error. NFEM: new method. HO-FEM: Characteristic based FEM.

where $r = \sqrt{x^2 + y^2}$, $\beta = 22.303$ and $T = 10$, producing maximum velocity $|\mathbf{u}|_{max}$ value of 50 at $r = 25$. We employ four structured meshes of linear triangular elements with element size lengths[3] and time step values of $\left\{\sqrt{2}, 0.005\right\}$, $\left\{\frac{\sqrt{2}}{2}, 0.0025\right\}$, $\left\{\frac{\sqrt{2}}{4}, 0.00125\right\}$ and $\left\{\frac{\sqrt{2}}{8}, 0.000625\right\}$, respectively. Reinitialization step parameters are $\varepsilon = 0.83\Delta l$ and $\Delta \tau = \alpha \frac{\Delta l^2}{8\varepsilon}$ (dummy time step), where Δl is the maximum triangle height and $\alpha = 0.1$. Simulation stops at the end of a cycle ($t = T$).

---

[3] Element size length is $\delta = \sqrt{\Delta x^2 + \Delta y^2}$; for 3D cases $\delta_{3D} = \sqrt{\Delta x^2 + \Delta y^2 + \Delta z^2}$ where Δx, Δy and Δz are size lengths of a cube composed by five tetrahedral cells (structured grids).
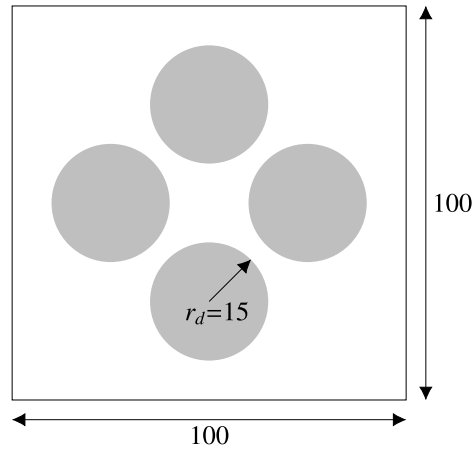
Fig. 6. Gaussian Vortex: Initial configuration.

Table 1
Gaussian Vortex. Errors at $t = T$.

Method	Mesh (δ)	$e(L_1^I)/l$	$e(L_1)$	$e(L_2)$	$\left|A_{0.5}^e\right|$ [%]	Mass error
NFEM	$\sqrt{2}$	1.682E−02	1.414E−01	2.329E−01	16.124	4.009E−15
	$\frac{\sqrt{2}}{2}$	8.647E−03	8.280E−02	1.700E−01	7.037	−1.644E−14
	$\frac{\sqrt{2}}{4}$	1.532E−03	4.642E−02	1.208E−01	0.383	−1.481E−13
	$\frac{\sqrt{2}}{8}$	6.068E−04	2.410E−02	8.461E−02	0.145	−8.923E−13
NFEM + Reinitialization	$\sqrt{2}$	2.684E−02	1.207E−01	2.681E−01	6.197	−5.291E−15
	$\frac{\sqrt{2}}{2}$	1.121E−02	4.894E−02	1.723E−01	1.579	−1.999E−14
	$\frac{\sqrt{2}}{4}$	3.084E−03	1.742E−02	9.116E−02	0.021	−1.653E−13
	$\frac{\sqrt{2}}{8}$	2.926E−04	5.979E−03	4.211E−02	0.000	−7.203E−13
Local calculation of normals	$\sqrt{2}$	2.761E−02	1.133E−01	2.792E−01	0.935	3.367E−15
	$\frac{\sqrt{2}}{2}$	1.199E−02	5.199E−02	1.794E−01	1.328	−1.628E−14
	$\frac{\sqrt{2}}{4}$	3.307E−03	1.898E−02	9.430E−02	0.072	−1.669E−13
	$\frac{\sqrt{2}}{8}$	3.046E−04	6.400E−03	4.219E−02	0.017	−1.197E−12

Results of the experiments for the four grids are summarized in Table 1. First column of Table 1 indicates the method, either NFEM as described by Eq. (19), or NFEM including reinitialization defined by Eqs. (20) and (21), or NFEM including reinitialization and local calculation of normals as reported in Section 2.4. Columns two to seven indicate average element side length δ, errors $e(L_1^I)/l$, $e(L_1)$, $e(L_2)$, $\left|A_{0.5}^e\right|$ %, and total mass error, respectively. Interface error $e(L_1^I)$ is defined as

$$e(L_1^I) = \frac{1}{L} \sum_{i=1}^{N} \left\{ \left| H\left(\hat{\phi}_i - \frac{1}{2} \right) - H\left(\phi_i - \frac{1}{2} \right) \right| (\mathbf{M}_L')_i \right\}, \tag{32}$$

and $\left|A_{0.5}^e\right|$ is the enclosed volume error defined as

$$A_{0.5}^e(t^n) = \frac{A_{0.5}(t^n) - A_{0.5}(t_0)}{A_{0.5}(t_0)}, \tag{33}$$

where $H(\cdot)$ is the Heaviside function, L is the interface length, ϕ is the theoretical solution, $(\mathbf{M}_L')_i$ is the nodal value of the lumped mass matrix, and t_0 is the initial time of the simulation; in Table 1, l is a characteristic length of the domain ($l = 100$). In the case of NFEM without reinitialization tool, $\hat{\phi}$ in Eq. (32) signifies final corrected solution. Interface length is computed at initial time and its value is 120π. The enclosed volume $A_{0.5}$ is computed as the area contained by the closed $\phi = 0.5$ contour, tracked by reconstructing the interface through elementwise linear interpolation.
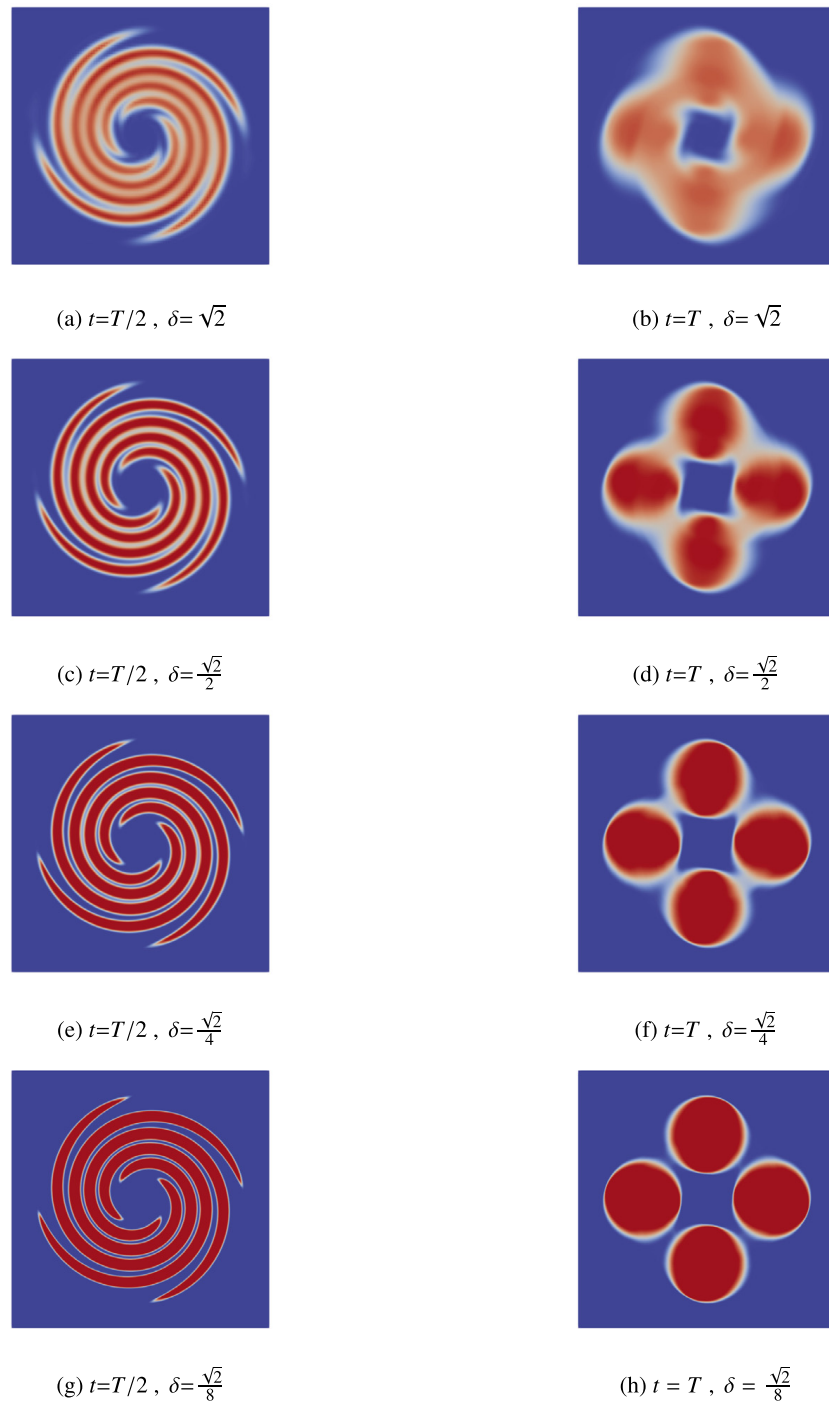
(a) $t=T/2$, $\delta=\sqrt{2}$

(b) $t=T$, $\delta=\sqrt{2}$

(c) $t=T/2$, $\delta=\frac{\sqrt{2}}{2}$

(d) $t=T$, $\delta=\frac{\sqrt{2}}{2}$

(e) $t=T/2$, $\delta=\frac{\sqrt{2}}{4}$

(f) $t=T$, $\delta=\frac{\sqrt{2}}{4}$

(g) $t=T/2$, $\delta=\frac{\sqrt{2}}{8}$

(h) $t=T$, $\delta=\frac{\sqrt{2}}{8}$

Fig. 7. Gaussian Vortex Test. Phase field ϕ. Transport results.

As can be expected, errors $e(L_1)$ and $e(L_2)$ diminish once mesh is refined (Table 1) for NFEM solution of transport equation (Figs. 7(a)–7(h)). Convergence order is lower than two mainly due to the presence of several quasi-discontinuities. Convergence order for interface error shows more irregular behavior, decreasing when finer meshes are used. Nevertheless, interface error lessens monotonically when element side length is reduced. A reason of this erratic behavior arises from the use of the Heaviside function in the error definition. Enclosed volume error oscillates, although it is bounded and decreases with finer meshes. This response is in accordance with discussion in Ref. [12] where enclosed volume error is related with value of ε. Hence enclosed volume error depends on the value of the maximum element size on the interface.

(a) $t=T/2$, $\delta=\sqrt{2}$

(b) $t=T$, $\delta=\sqrt{2}$

(c) $t=T/2$, $\delta=\frac{\sqrt{2}}{2}$

(d) $t=T$, $\delta=\frac{\sqrt{2}}{2}$

(e) $t=T/2$, $\delta=\frac{\sqrt{2}}{4}$

(f) $t=T$, $\delta=\frac{\sqrt{2}}{4}$

(g) $t=T/2$, $\delta=\frac{\sqrt{2}}{8}$

(h) $t=T$, $\delta=\frac{\sqrt{2}}{8}$
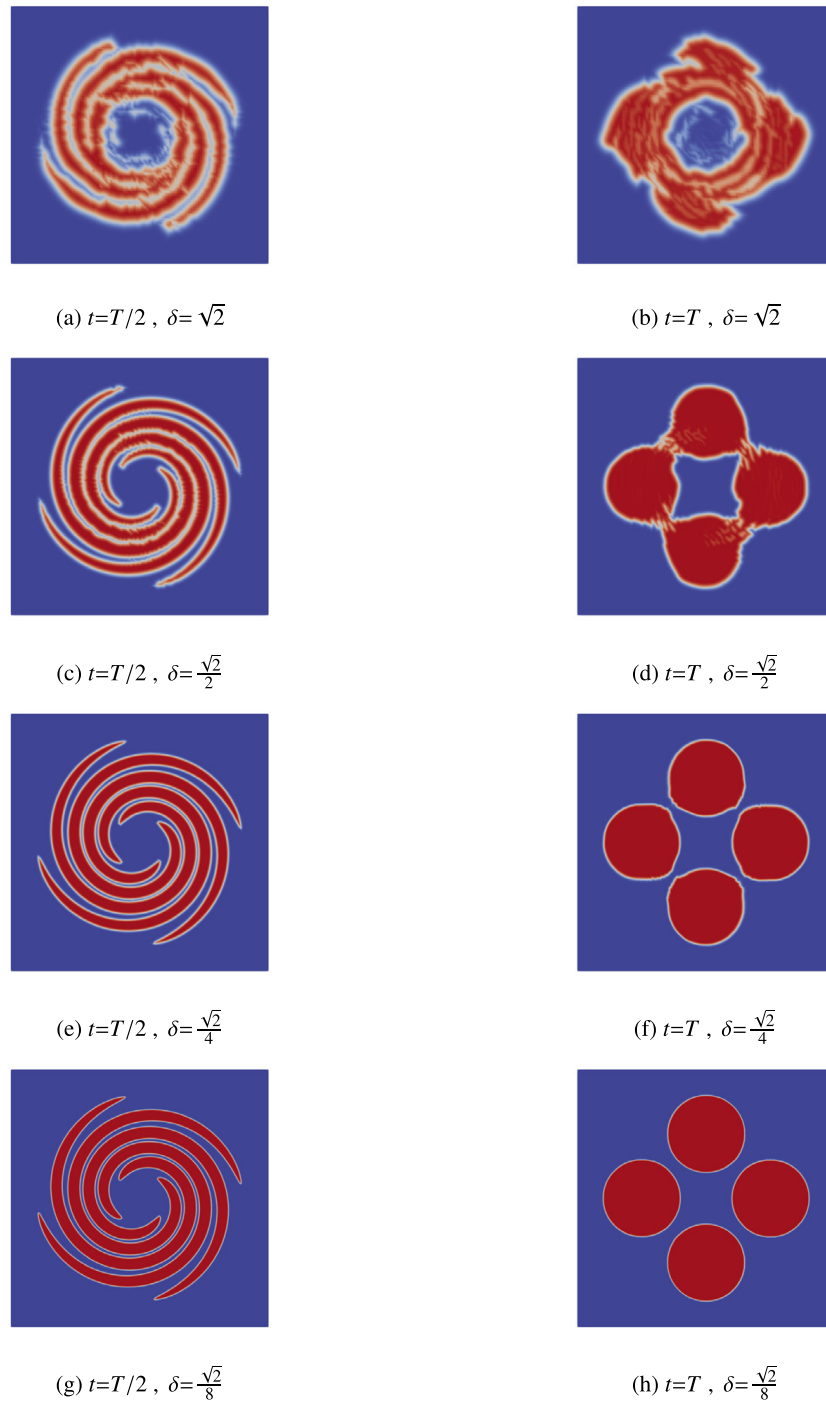
Fig. 8. Gaussian Vortex Test. Phase field ϕ. NFEM+Reinitialization results.

Errors behave in a similar manner when reinitialization is active (see Figs. 8(a)–8(h) and second row of Table 1). Decrease in $e(L_1)$ and $e(L_2)$ is noticeable in fine grids, up to four times. Otherwise, reinitialization process is not efficient for low mesh resolution: reader can observe in Table 1 that $e(L_2)$ for the coarsest mesh is higher when we use reinitialization. Although now interface error is marginally higher for coarse meshes, for the finest mesh this error diminishes substantially. Besides, enclosed volume errors with reinitialization exhibit values nearly an order of magnitude lower for all the resolutions. This enhancement is due to the artificial compression effect in the reconstruction, reducing extra diffusion originated in the transport step. Local computation of normals does not introduce relevant further amelioration because interfaces are too close, and there are not regions in the vicinity

Table 2
Sphere in a transient swirling deformation flow. Errors at $t = T$.

Method	δ_{3D}	$e(L_1^I)/l$	$e(L_1)$	$e(L_2)$	$|A_{0.5}^e|$ [%]
NFEM	$\sqrt{3}$	9.332E−03	9.694E−03	5.632E−02	13.950
	$\frac{2\sqrt{3}}{3}$	5.397E−03	6.826E−03	4.597E−02	5.191
	$\frac{\sqrt{3}}{2}$	3.786E−03	5.338E−03	4.015E−02	2.954
NFEM + Reinitialization	$\sqrt{3}$	8.995E−03	6.029E−03	4.416E−02	12.238
	$\frac{2\sqrt{3}}{3}$	5.663E−03	4.377E−03	3.603E−02	7.062
	$\frac{\sqrt{3}}{2}$	4.069E−03	3.497E−03	3.093E−02	4.509
Local calculation of normals	$\sqrt{3}$	6.729E−03	4.214E−03	3.874E−02	3.849
	$\frac{2\sqrt{3}}{3}$	3.945E−03	2.838E−03	3.059E−02	2.407
	$\frac{\sqrt{3}}{2}$	2.748E−03	2.359E−03	2.582E−02	1.750
Guermond et al. [22]	$\sqrt{3}$	6.943E−02	–	–	4.179
	$\frac{\sqrt{3}}{2}$	6.329E−03	–	–	0.481

of interfaces with (approximately) constant values of the phase function. Overall results reveal that coarsest mesh ($\delta = \sqrt{2}$) has not sufficient resolution for a competent usage of reinitialization tools in long term calculation for this severe test (see Figs. 7(b) and 8(b)). Without reinitialization, finest resolution is needed ($\delta = \sqrt{2}/8$) to avoid spurious coalescence of disks (see Fig. 7(h)). Instead, for NFEM plus reinitialization, $\delta = \sqrt{2}/4$ (see Fig. 8(f)) is enough to prevent merging of disks.

3.3. Sphere in a transient swirling deformation flow

The experiment was proposed by Leveque [31]. A sphere of diameter 30 is placed at initial time with its center at $(-15, -15, -15)$ in a $[-50, 50] \times [-50, 50] \times [-50, 50]$ domain. The periodic advective velocity field has the following Cartesian components

$$u(\mathbf{x}, t) = 200 \sin\left(\frac{\pi(x+50)}{100}\right)^2 \sin\left(\frac{2\pi(y+50)}{100}\right) \sin\left(\frac{2\pi(z+50)}{100}\right) \cos\left(\frac{\pi t}{T}\right),$$

$$v(\mathbf{x}, t) = -100 \sin\left(\frac{2\pi(x+50)}{100}\right) \sin\left(\frac{\pi(y+50)}{100}\right)^2 \sin\left(\frac{2\pi(z+50)}{100}\right) \cos\left(\frac{\pi t}{T}\right),$$

$$w(\mathbf{x}, t) = -100 \sin\left(\frac{2\pi(x+50)}{100}\right) \sin\left(\frac{2\pi(y+50)}{100}\right) \sin\left(\frac{\pi(z+50)}{100}\right)^2 \cos\left(\frac{\pi t}{T}\right),$$

where $T = 3$. The largest deformation of the sphere takes place at $t = T/2$ (Fig. 9(b)), while at $t = T$ the sphere recovers the initial state. We use three structured meshes of four nodes tetrahedral elements with element size length and time step $\left\{\sqrt{3}, 0.002\right\}$, $\left\{\frac{2\sqrt{3}}{3}, 0.001333\right\}$, and $\left\{\frac{\sqrt{3}}{2}, 0.001\right\}$, respectively. To achieve sufficient resolution of thin filaments, $\varepsilon = 0.50\Delta l$, and $\Delta\tau = \alpha\frac{\Delta l^2}{8\varepsilon}$ (dummy time step), where Δl is the maximum tetrahedral height and $\alpha = 0.1$. Interface (area) $L = 900\pi$.

Table 2 shows errors at $t = T$, ($l = 100$), with the same arrangement as Table 1. We have added results from Ref. [22], where a modified conservative level set method by antidiffusion techniques has some comparable spatial and temporal discretization features with the present model. For the results given in Ref. [22] we indicate in second column the resulting equivalent element size lengths for a proper comparison, given that discretizations do not match exactly.

Reinitialization diminishes $e(L_1)$ and $e(L_2)$ as in the Gaussian vortex test. However a regularization of normals improves the performance. For instance, with the intermediate mesh ($\delta_{3D} = 2\sqrt{3}/3$) and local calculation of normals (see Table 2, ninth row) results are better than with the fine mesh ($\delta_{3D} = \sqrt{3}/2$) with standard normal usage (see Table 2, seventh row). Interface error and enclosed volume error decrease once local calculation of normals is active (see Table 2, third, sixth and ninth rows). Besides, this tool reduces $e(L_1)$ and $e(L_2)$ attained by reinitialization. Sharp interfaces are not as close as in the previous experiment, hence action of normal local calculation avoids
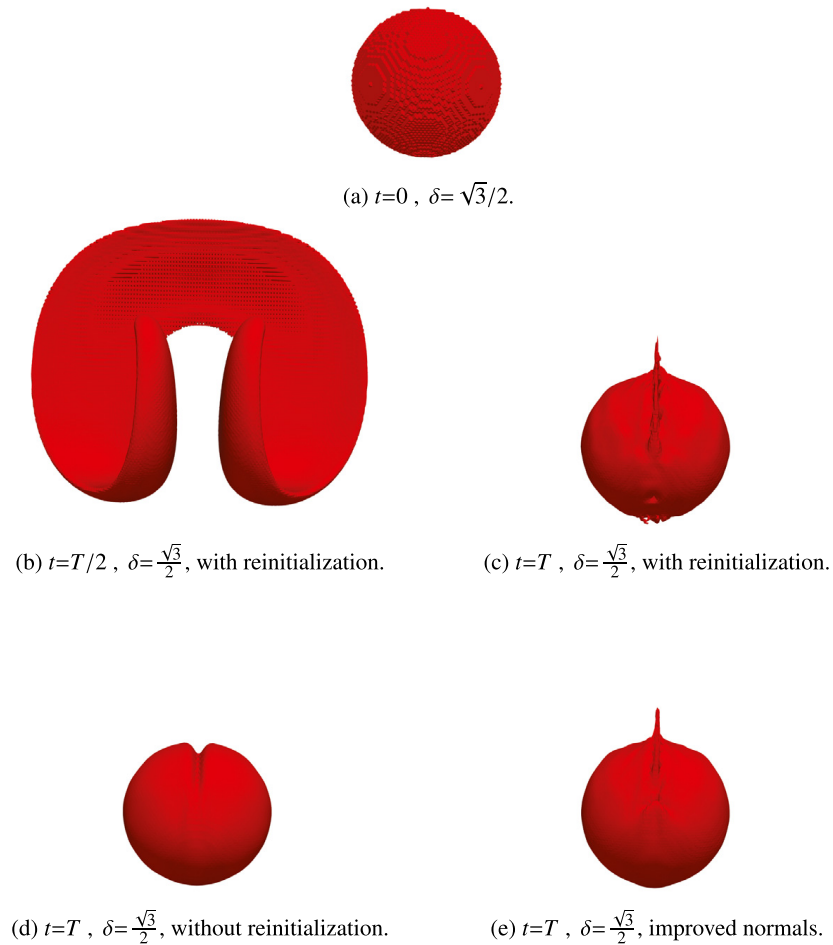
(a) $t=0$, $\delta= \sqrt{3}/2$.

(b) $t=T/2$, $\delta=\frac{\sqrt{3}}{2}$, with reinitialization.

(c) $t=T$, $\delta=\frac{\sqrt{3}}{2}$, with reinitialization.

(d) $t=T$, $\delta=\frac{\sqrt{3}}{2}$, without reinitialization.

(e) $t=T$, $\delta=\frac{\sqrt{3}}{2}$, improved normals.

Fig. 9. Sphere in a transient swirling deformation flow. Surface $\phi = 1/2$. (b) and (c) with reinitialization. (d) without reinitialization. (e) local calculation of normals.

the indeterminacy far from the interface in a more efficient way, and reduces wiggles of phase function in the vicinity of interfaces. Interface error is smaller compared with Ref. [22] for the coarse and intermediate mesh, and results are marginally better for the coarse mesh in terms of enclose volume error. Enclosed volume error diminishes substantially for intermediate mesh and fine mesh, although somewhat higher than finite volume results from Ref. [22]; nevertheless in this test the model reported in [22] does not preserve sign. Total mass errors (not reproduced in Table 2) are of the same order as those displayed in Table 1.

To capture the thinnest pattern of the deformed state (Fig. 9(b)) it is necessary the finest mesh. Slight oscillations on the interface (Fig. 9(c)) are substantially reduced by the beneficial effect of local calculation of normals (Fig. 9(e)). On the other hand, at the end of the cycle some kind of crest attached to the sphere appears, ascribable to a secondary effect of the reinitialization, which moves artificially the interface. This anomaly can also be observed in other models (see e.g. [39]), but was not detected in the remaining experiments. In fact these deviations, as well as wiggles, do not appear for transport equation solution without reconstruction (see Fig. 9(d)).

3.4. Dam break with obstacle

The experiment [32] is performed in a tank of $3.22 \times 1 \times 1$ m, where a closed gate retains a steady volume of water of $1.228 \times 1 \times 0.55$ m (0.6754 m^3). A fixed brick of size $0.161 \times 0.403 \times 0.161$ m is placed with its centroid at 1.248 m downstream of the gate axis. Test starts by releasing the water almost instantaneously. Figs. 10, 11 and 12(a) sketch the geometry and initial condition. Fig. 10 also indicates as H1, H2, H3, and H4 the positions of height measurements, while Fig. 11 depicts the brick and the positions of pressure gauges, indicated as P1 to P8. In the numerical test we employ a structured grid of linear tetrahedrons with $202 \times 64 \times 63$ nodes. Slip boundary
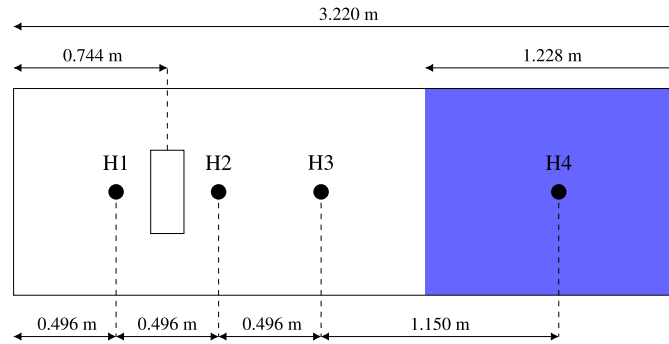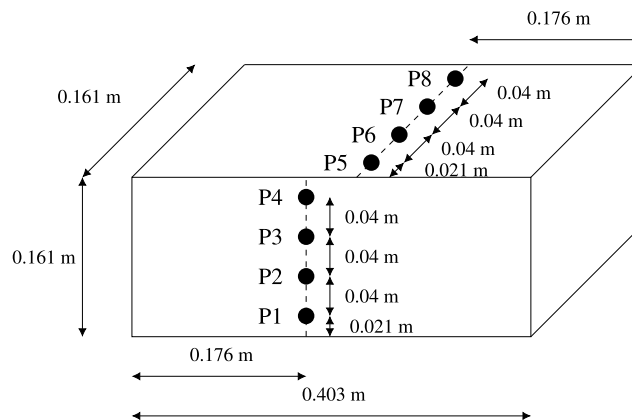
Fig. 10. Dam break with obstacle. Set up.

Fig. 11. Dam break with obstacle. Geometry of the obstacle.

condition was prescribed on the boundaries. Time increment is $\Delta t = 0.001$ s, time integration parameter $\theta = 1$, $\varepsilon = 0.67\Delta l$ and $\Upsilon = \Delta l/(6\varepsilon)$ (see definition of Υ in Section 2.5); for the computation of regularized normals we use two element levels. Density ratio is $\rho_1/\rho_2 = 0.001$ and surface tension coefficient $\sigma = 0.07$ N/m; viscosity ratio value is assumed as $\mu_1/\mu_2 = 0.01$, to be consistent with results of other models (see e.g. Ref. [40]).

Figs. 12(a)–12(e) show some interesting snapshots of the simulation at times $t = 0$ (initial), 0.4 s, 0.6 s, 1.1 s and 2.0 s, respectively. In Fig. 12(b) it is seen the propagation of the initial wave over the dry bed before the impact against the brick, while in Fig. 12(c) it is recognized when the discharge overflows the block, and is advancing towards the left wall, reaching it at time of around 0.8 s. After the impact on the left wall the reflected wave travels back and, at the same time, relevant momentum transfer from horizontal to vertical occurs in the obstacle (see Fig. 12(d)). Fig. 12(e) depicts backing wave submerging the obstacle at $t = 2.0$ s.

Figs. 13–18 plot the history $p(t)$ (pressure) at the points P1, P3, P5, and P7, and the history $h(t)$ (height of water) at the points H2 and H4, respectively, for experimental measurements and computed values. First pressure peak at point P1 is precisely captured in phase and amplitude (Fig. 13). Pressure computation at point P3 is also very precise in phase, but amplitude is somewhat underpredicted, mainly due to limitation of the grid resolution to simulate a proper momentum transfer from horizontal to vertical in the vicinity of the brick wall. It is interesting to note that this reduction of pressure is also observed in other works (e.g. [32,40]). Computation matches with experimental for P1 and P3 up to $t = 4.5$s, covering a complete travel of primary and secondary waves, and a relevant part of the second travel after reflection on the right wall. A small delay appears in the second impact ($t \approx 5$ s) (as in models referenced above). Pressure computations over the brick (points P5 and P7, see Figs. 15, 16) are adequate, although the first peak is slightly overpredicted. However, at the top of the obstacle an intense mixing of water/air occurs, yielding a foreseeable detachment of numerical calculations from local pressure measurements. Some oscillations in the pressure, existing in the physics (see Figs. 15 and 16), and in water heights (Fig. 17) are amplified to a limited degree by the numerical solution. These deviations from real oscillations are attributed to an insufficient interface resolution in the vicinity of the obstacle, where an intense and diffuse water/air mixing
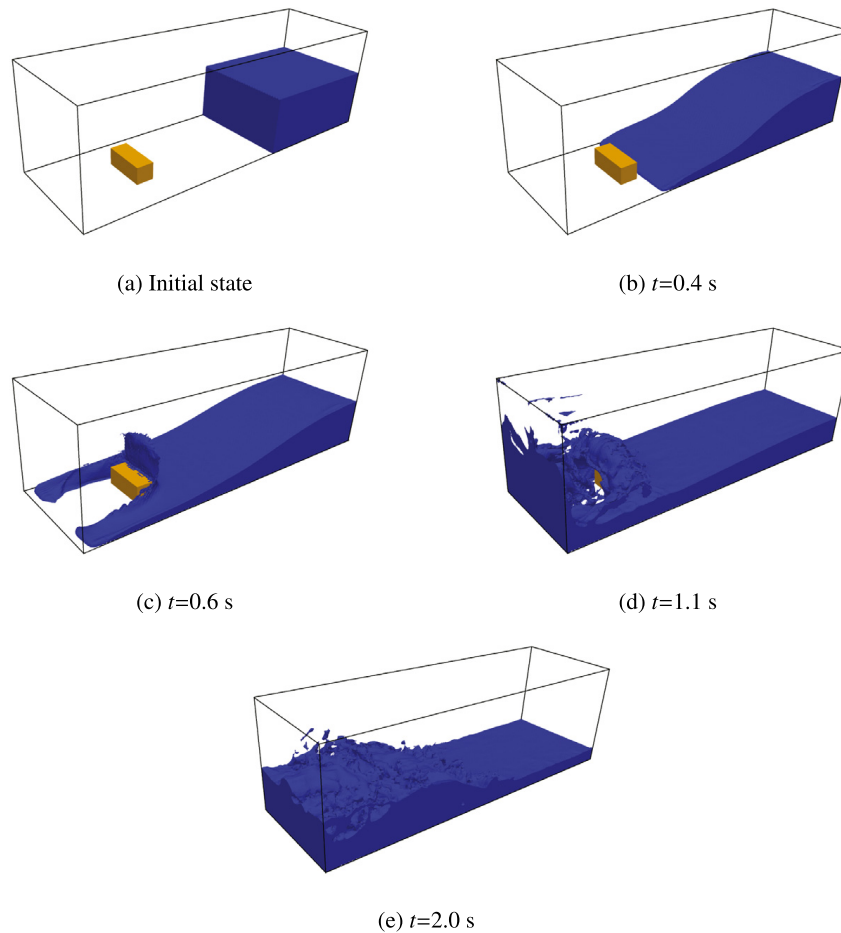
(a) Initial state

(b) t=0.4 s

(c) t=0.6 s

(d) t=1.1 s

(e) t=2.0 s

Fig. 12. Dam break with obstacle.

occurs when water collides the brick (see e.g. Fig. 12(e)). In the case of measurement points P5 and P7, the vortex shedding created on the brick edge also contributes to spread water in the vicinity of the brick.

Water height results show good agreement with measurements in terms of celerity of the wave traveling on a dry bed (first peak is again precisely catched (see Fig. 17)), and in terms of elevations in the expansion wave region (see Fig. 18). Peaks are very accurately detected in the first travel. Of course, a small delay in the second peak appears, consistent with pressure output. Reader can observe the good capture of the returning wave front at H4 (at around $t = 2.7$ s) in Fig. 18. Water heights computed by a NFEM depth integrated model [41] are remarkable close (see output in [16], pp 66–67). Nevertheless, although some phase and amplitude errors at peaks are lower, pressure computation is not sufficiently accurate in the neighborhood of the block for the depth integrated model, as might be expected.

3.5. Emergence of cavities and geysering in ducts

We discuss intrusion of cavities in ducts in the following three subsections, according with three stages of the study. First stage concerns the study of a large air pocket intruding a horizontal duct when a weir is located across the open end of the conduit (see sketch in Fig. 19). Second subsection scrutinizes conditions for the formation of air cavities by combining partial closure of the gate and duct slope. Third subsection focuses on momentum transfer between a horizontal duct with the presence of an air cavity and a vertical duct with still water (see sketch in Fig. 25), and the rising of the bubble along the vertical duct. By this sequence of three tests, numerical study covers the comparison with laboratory experiments concerning propagation of air cavity [1,2], emergence of close cavities [3], vertical propagation of bubbles in vertical tubes [4] and geysering on top of the conduit.
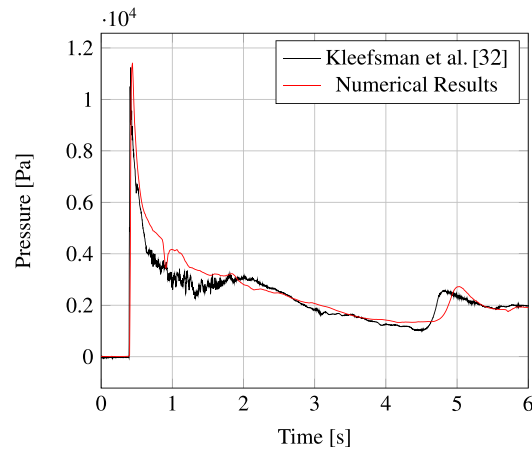
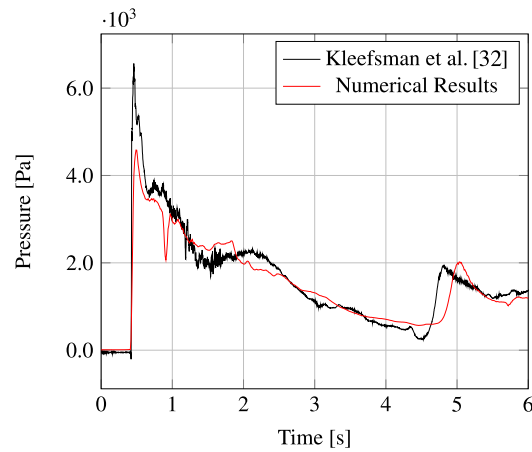**Fig. 13.** Experimental and numerical results. Pressure at P1.

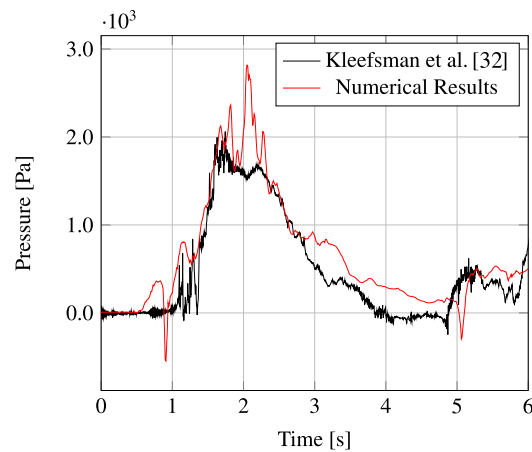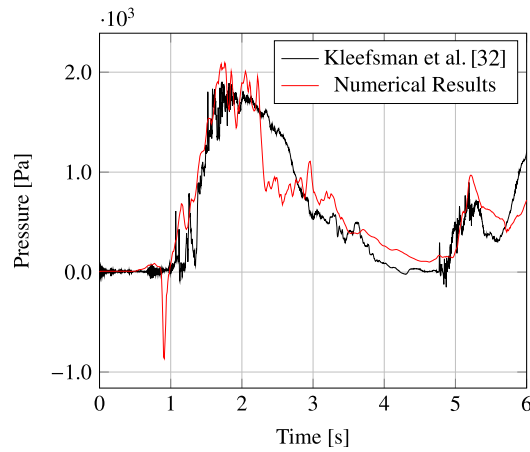**Fig. 14.** Experimental and numerical results. Pressure at P3.

Fig. 15. Experimental and numerical results. Pressure at P5.

3.5.1. Air cavities in horizontal ducts

The experiment consists of a rectangular duct of length 1.50 m and height $d = 0.10$ m, with a gate of variable height at the end, where a chamber of 0.20×0.20 m is used to drain water (Fig. 19). Duct is filled with water and gate is locked. At initial time, gate is suddenly unlocked up to a partial opening by moving it down. Then water

Fig. 16. Experimental and numerical results. Pressure at P7.
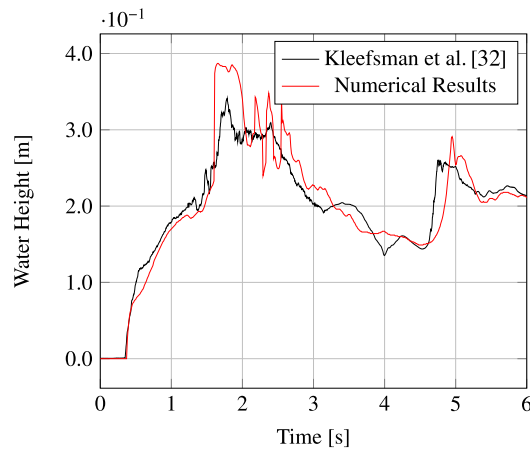
Fig. 17. Experimental and numerical results. Water height at H2.
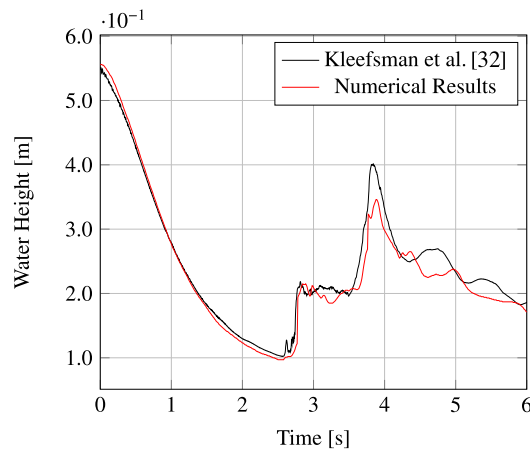
Fig. 18. Experimental and numerical results. Water height at H4.

starts to drain and air starts to fill the evacuated water volume. Both fluids are assumed incompressible, $\rho_1/\rho_2 = 0.001$, $\mu_1/\mu_2 = 0.01$, $|\mathbf{g}| = 9.81$ m/s^2, and $\sigma = 0.07$ N/m. Tests were conducted for gate heights $w = 0$, $0.2d$, $0.3d$, $0.4d$, $0.5d$, $0.6d$ and $0.7d$. Average element length for the grid in the series is $\delta = 0.002\sqrt{2}$ m, $\theta = 1$, and $\Delta t = 1 \cdot 10^{-4}$ s. Simulations stop at 3 s. Reinitialization parameters are $\varepsilon = 0.83\Delta l$ and $\Delta\tau = 0.1\Delta l^2/(8\varepsilon)$. Slip
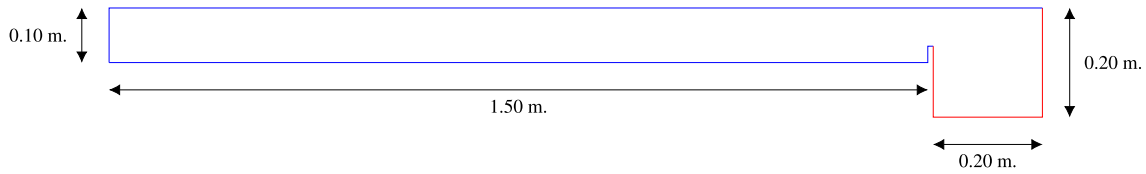
Fig. 19. Domain for air cavities simulations. Blue color boundary: Slip condition; red color boundary: inlet/outlet condition. (For interpretation of the references to color in this figure legend, the reader is referred to the web version of this article.)
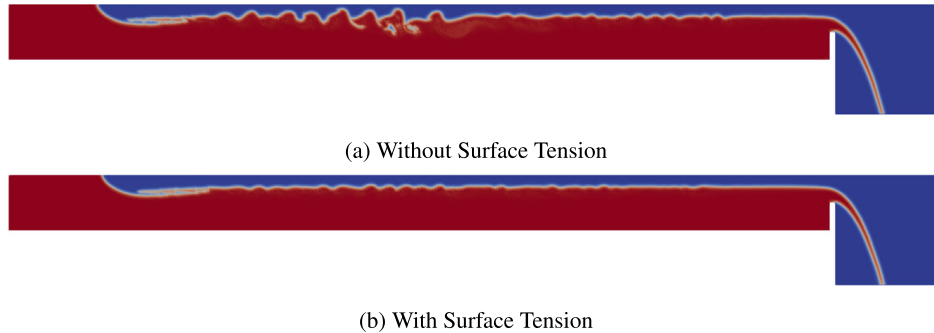

(a) Without Surface Tension

(b) With Surface Tension

Fig. 20. Air cavity simulation for a horizontal duct with $w = 0.5d$. Phase function at $t = 3$ s.

condition is applied on solid walls (blue in Fig. 19). We assume free velocity, $p = 0$, $\partial p / \partial \mathbf{n}_b = 0$, and $\phi = 0$ on inlet/outlet boundaries (red in Fig. 19); hence if $\mathbf{u} \cdot \mathbf{n}_b < 0$, air flows into the domain. These conditions have proven to be effective to discharge the water jet, practically unaltered by the presence of the boundary; besides, conditions facilitate air entrance and avoid spurious vortices and negative values of pressure in the jet body.

When the gate is partially closed, a bore is developed downwind the front of the cavity (see e.g. Fig. 20). Cases considered in the numerical tests and in the laboratory [2] have a bore formation with low (supercritical) Froude number, with jumps going from prejump type, to undular type and to transition regime. For these Froude number ranges, free surface in the subcritical region is highly oscillating. However, grids did not include interface refinement because surface tension is sufficient to obtain a stable free surface (see illustration in Fig. 20). Surface tension can reduce cavity celerity and can affect slightly the shape of the front (see e.g. [2] and references therein), but its overall impact is not significant. The resolution parameter (Section 2.5) is chosen with the value $\Upsilon = \Delta l/(30\varepsilon)$. Very low values of Υ originate an overestimation of bore celerity. Nevertheless, cavity celerity appears to be independent of resolution parameter. This is probably due to the behavior of the cavity in the supercritical region, close to a potential flow.

Fig. 21 depicts normalized cavity celerity $F = c/\sqrt{gd}$, where c is the cavity celerity, and normalized bore celerity $F_b = c_b/\sqrt{gd}$, where c_b is the bore celerity, in terms of downstream water depth ratio $H_2 = h_2/d$; the depth h_2 is measured downstream the bore. Black marks indicate experimental measurements in Ref. [2], and red marks indicate numerical output; cross sign corresponds to bore celerity, while circle sign corresponds to cavity celerity. Finally, solid line represents the historical theoretical results by Benjamin [1], and dashed lines represent theoretical results in Ref. [2], taking into account surface tension and stagnation point position effects. Cavity front location and bore location were tracked each 0.5 s in the interval $[0, 3]$ s. Discrepancies between experimental results and numerics are small for values of bore celerity. Numerical results are slightly higher than measurements, but these differences are always less than 5% in comparison with laboratory results. Besides, for unsteady regime (i.e., when bore and cavity have different celerities), bore celerity model results are in good agreement with measurements.

3.5.2. Air cavities in sloping ducts

We perform two series of experiments for ducts with slope and partial opening of the final gate. First series is defined by $w = 0.2d$, $0.3d$, $0.4d$, and slopes 2%, 5% and 7%; second series is defined by $w = 0.5d$, $0.6d$, $0.7d$, and slopes 1%, 2% and 3%. For the second series, interface is close to the top of the pipe and high air acceleration
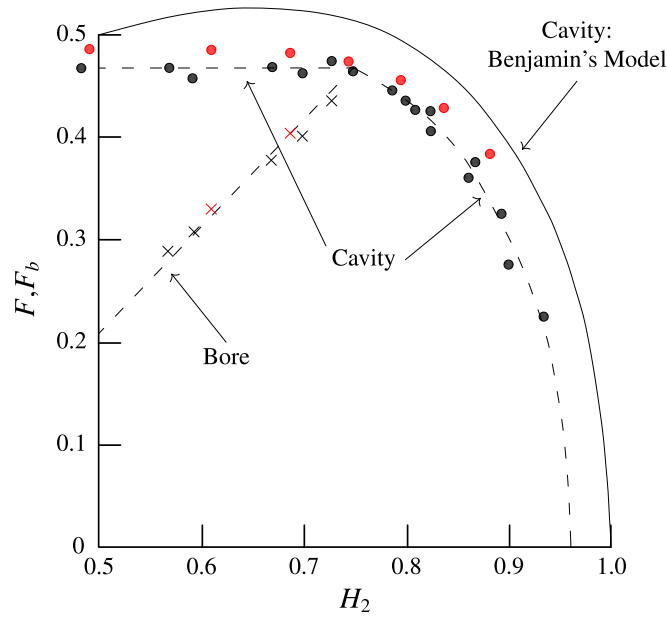
Fig. 21. Cavity and bore normalized celerities as function of downstream water depth ratio. Red marks: numerical results; black marks: experimental [2]. Solid line: theoretical [1]; dashed line: theoretical [2]. $F = c/\sqrt{gd}$, $F_b = c_b/\sqrt{gd}$, $H_2 = h_2/d$, c_b is the bore celerity and h_2 is the flow depth downstream the bore. (For interpretation of the references to color in this figure legend, the reader is referred to the web version of this article.)

yields very unstable interfaces. For both situations, $\Upsilon = \Delta l/(300\varepsilon)$ and local mesh refinement is implemented. Fig. 22 illustrates the effect of reducing interface thickness by refinement. Without refinement, a fictitious sealing of the cavity takes place due to unphysical perturbations along the free surface; sealing does not occur in laboratory experiments for this set-up [3].

Numerical and experimental results are shown in Fig. 23. Black color indicates laboratory output, circles mark when sealing does not occur, while squares and crosses mean that cavity seals at irregular or regular intervals, respectively. Red denotes numerics, crosses denote cavity sealing, and circles denote open cavity. A special experiment is pointed out by diamond sign. In this case, a splash of water touches the top of the duct, occurring just after state depicted in Fig. 24(a). Though resulting air bag is isolated from atmosphere, it cannot be considered as a meta-stable state. Triangles show those cases in which the bore advances away the outflow end of the conduit. Here, downstream flow depths continue to rise (see Fig. 24(b)). Although duct length is not long enough to capture the sealing for configurations denoted by the triangles, sealing occurrence is assured for longer ducts. Finally, dotted black line in Fig. 23 is an interpolation of both experimental and numerical outputs. Line displays limiting conditions for sealing in terms of gate opening and slope. It is noted that numerical results for sealing development are fairly close to those observed in the laboratory.

3.5.3. Bubble rising in vertical ducts

The dynamics of ascension to the free surface of large air bubbles along a vertical duct normally requires a three-dimensional simulation. In Refs. [42,43] authors substantiate this requisite by computing the non-dimensional rising velocity of purely inertial Taylor bubbles for plane and axisymmetric cases. Results reveal a significant difference between both premises: values of velocities are $w_b/\sqrt{gd_d} = 0.240$ for plane bubbles, and 0.345 for axisymmetric ones, much closer to experimental observations; w_b is the rising velocity and d_d is the vertical duct diameter. In this study we focus on the coupling of the bubble head and the free surface progression, without the need of details in geometrical features of the bubble provided by the full three-dimensional procedure. Hence, problem is assumed as axisymmetric and an ad-hoc model complementary to the complete 3D model has been developed. Nevertheless, for completeness, a full 3D case of the problem has been performed and discussed at the end of this subsection.

Axisymmetric formulation is obtained from conservation equations in cylindrical coordinates (e.g. Ref. [44]), by neglecting terms in the azimuthal direction and derivatives with respect to the azimuthal coordinate. For the sake of brevity, complete Galerkin spatial discretization is not included, given its similarities with the method stated
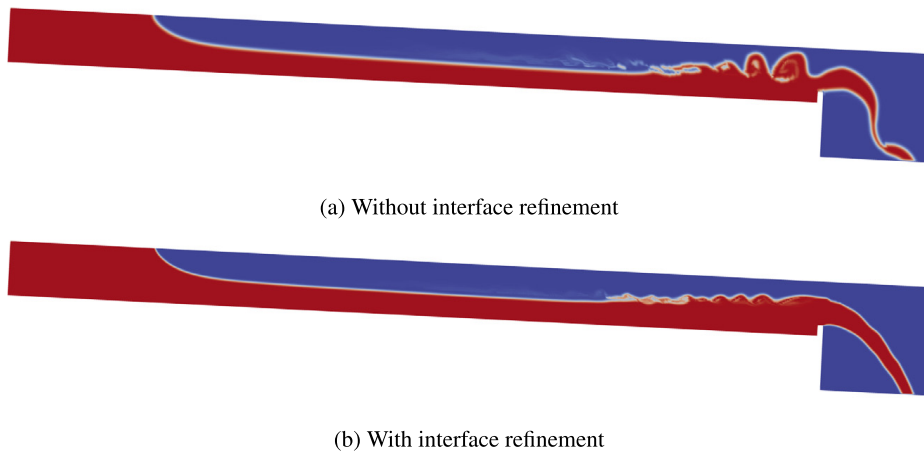
(a) Without interface refinement

(b) With interface refinement

Fig. 22. Air cavity simulation results for a duct with 5% slope and $w = 0.2d$. Phase function at $t = 2.5$ s.
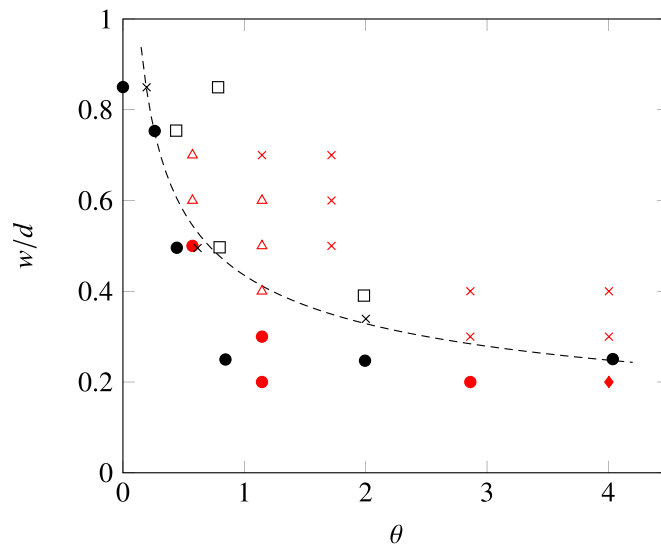

Fig. 23. Cavity sealing as function of w/d and slope θ (in degrees). Comparison between experimental output [3] (black marks) and numerical results (red marks). (For interpretation of the references to color in this figure legend, the reader is referred to the web version of this article.)
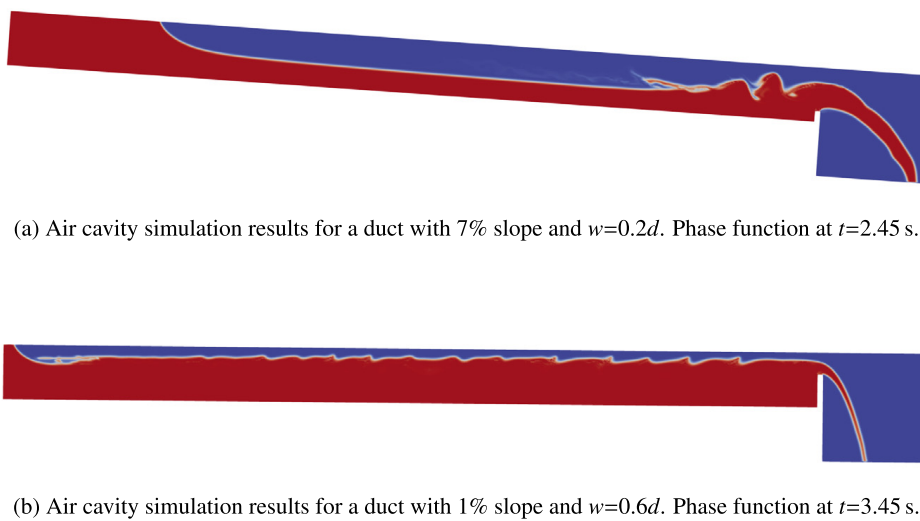

(a) Air cavity simulation results for a duct with 7% slope and $w=0.2d$. Phase function at $t=2.45$ s.

(b) Air cavity simulation results for a duct with 1% slope and $w=0.6d$. Phase function at $t=3.45$ s.

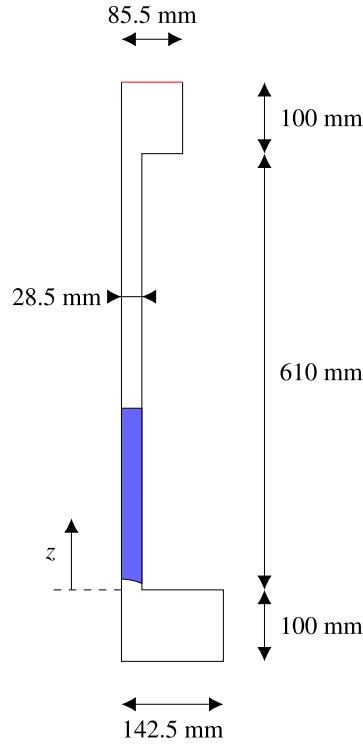**Fig. 24.** Air cavity simulation results for a duct with 7% slope and 1% slope.

Fig. 25. Geysering Test. Sketch and dimensions. (For interpretation of the references to color in this figure legend, the reader is referred to the web version of this article.)

by Eqs. (5), (6) and (7) for the high order procedure, and by Eqs. (13) and (14) for the low order procedure. To highlight distinctions between the axisymmetric approximation and the original high order solution, phase field advection is considered (see Eq. (8)). Solution of phase function is defined by the finite element spaces $\mathcal{W}^h \subset \mathcal{W} = \{w \in H^1(\Omega) \mid w = 0 \text{ on } \Gamma_\phi^-\}$ and $\Phi^h \subset \Phi = \{\phi \in H^1(\Omega) \mid \phi = \overline{\phi} \text{ on } \Gamma_\phi^-\}$, and is formulated as: Find $\phi^h \in \Phi^h$ such that

$$
\left(rw^h, \frac{\Delta\phi^h}{\Delta t} \right)_\Omega = \left(\mathbf{u}_o \cdot \nabla_o w^h, r\phi^h \right)_\Omega^n - \frac{\Delta t}{2} \left\{ \left\langle r\nabla_o \cdot \left(w^h \left(\mathbf{u}_o^h \mathbf{u}_o^h \right)^{n+1/2} \right), \nabla_o(\phi^h)^n \right\rangle_{\Omega_I} \right.
$$
$$
- \left\langle rw^h \left((\mathbf{u}_o^h)^{n+1/2} \cdot \nabla_o(\mathbf{u}_o^h)^n \right), \nabla_o(\phi^h)^n \right\rangle_{\Omega_I} + \left(r\nabla_o \cdot \left(w^h (\mathbf{u}_o^h)^{n+1/2} \right), \left(\phi^h \nabla_o \cdot \mathbf{u}_o^h \right)^n \right)_{\Omega_I} \right\}
$$
$$
- \left[w^h, r\phi^h \mathbf{u}_o \right]_{\Gamma+}^n - \left[w^h, r\overline{\mathbf{q}}_\phi \right]_{\Gamma_q^-}^n , \quad \forall \, w^h \in \mathcal{W}^h .
\tag{34}
$$

where r is the radial coordinate, $\mathbf{u}_o = (u_r, u_z)$, u_r, u_z are radial and axial velocity components, respectively, and differential volume is $2\pi r \mathrm{d}\Omega$, in agreement with notation given after Eq. (6). In Eq. (34), operators $\nabla_o f = \frac{\partial f}{\partial r}\mathbf{r} + \frac{\partial f}{\partial z}\mathbf{z}$, and $\nabla_o \cdot \mathbf{f}_o = \frac{1}{r}\frac{\partial(rf_r)}{\partial r} + \frac{\partial f_z}{\partial z}$, where f is a scalar field and $\mathbf{f}_o$ is a vector field.

Bubble dynamics is mainly governed by three elements, the imbalance between air pressure and water column height, the water film attached to the duct wall, and the air compression/expansion due to the surrounding water [4]. To simulate adequately internal air pressure, compressible model is active. If the model operates on the assumption that fluids are incompressible, initial air pressure is automatically overwritten by hydrostatic pressure of the liquid phase, and the bubble acquires a low rising velocity because air expansion is not taken into account. Thus free surface keeps nearly static as a consequence of the resulting weak momentum transfer, contradicting laboratory and in-situ observations.

We reproduce a selected experiment of Ref. [4], where authors investigate release of air and water through ventilation towers. Experiment consists of a vertical tube of diameter $d_d = 0.057$ m and length $L_d = 0.610$ m connected below to a horizontal duct of 0.094 m diameter. The initial time is considered when air reaches entrance of the vertical pipe (zero height). At this initial stage, vertical duct is filled of water up to a height of 0.254 m,

while horizontal duct is filled with air with a relative pressure of 2452.5 Pa (0.25 meters of water column). The experiment is repeated three times in the laboratory. Domain for this simulation is depicted in Fig. 25. It has two chambers, the upper one allows air to enter and leave the vertical duct, and the lower one contains the air bubble. Lower chamber has a height of 0.1 m. Although this value is close to the diameter of the horizontal tube in the laboratory experiment, it is not relevant to the test to replicate exactly laboratory size of the horizontal tube, as long as air volume is sufficient to originate the bubble. Initial conditions are established as follows. Water volume reaches level $z = 0.254$ m, and lower water/air interface is an arch of circle with radius of 0.07 m and its center situated at $z = -0.055$ m. This shape is imposed to help bubble genesis, avoiding indeterminacy at initial steps. Reference densities are $\rho_1 = 1.225$ kg/m^3, $\rho_2 = 1000$ kg/m^3, viscosities are $\mu_1 = 1.8 \cdot 10^{-5}$ kg/(ms), $\mu_2 = 1 \cdot 10^{-3}$ kg/(ms), surface tension coefficient is $\sigma = 0.07$ N/m, and $| \mathbf{g} | = 9.81$ m/s^2. Celerity values are $a_1^2 = 1.0 \cdot 10^5$ m^2/s^2, $a_2^2 = 2.2 \cdot 10^6$ m^2/s^2. We employ a structured mesh with $\delta = 0.00114\sqrt{2}$ m and a time step $\Delta t = 1.25 \cdot 10^{-5}$ s. Reinitialization parameters are $\varepsilon = 0.83\Delta l$ and $\Delta\tau = 0.1\Delta l^2/(8\varepsilon)$, and $\Upsilon = \Delta l/(1200\varepsilon)$. This value of Υ proves to be adequate to alleviate spurious momentum transfers between air and the thin water layer attached to the vertical duct wall. Boundary marked with red in Fig. 25 has inlet/outlet boundary condition, as described in Section 3.5.1; remaining boundaries have slip condition. No additional conditions are necessary for boundaries coinciding with axisymmetry axis.

Numerical and experimental non-dimensional results for the three runs are superimposed on Fig. 26. Figure depicts history of bubble head position z_b (Fig. 26(a)), free surface height z_{fs} (Fig. 26(b)), and bubble pressure H_p (measured in height of water column) (Fig. 26(c)), where $\{z_b^*, z_{fs}^*, H_p^*\} = \{z_b, z_{fs}, H_p\}/L_d$, and $t^* = t\sqrt{gd_d}/L_d$. There are appreciable differences among laboratory series due to fluctuations in the valve opening at early stages of experiments. After initial transients during bubble formation, numerical output shows a quasi-constant bubble celerity, with a good agreement with the three laboratory series (Fig. 26(a)). Experimental tests also evince a strong dependency of free surface vertical displacement on initial conditions, particularly on the phase of its oscillations. This uncertainty makes difficult a proper comparison with numerics. Nevertheless free surface numerical answers show a proper capture of its history, situated nearly always in the experimental range (Fig. 26(b)); when bubble head gets close to the water free surface, the model slightly overpredicts position of the free surface. Furthermore, bubble release in the laboratory is consequential in inner bubble pressure fluctuations [4]. Fluctuations are visible in model results (Fig. 26(c)), suggesting a realistic coupling between fluids due to the weakly compressible premise. Numerical answers are again in the range of experimental results.

Last numerical experiment is the assessment of water return to the street level due to the rise of air pockets in vertical pipes, often called *geysering*. Layout of computational domain is similar to previous one (Fig. 25). Now, vertical conduit has 4.0 m length, 0.5 m diameter and it is filled of water up to a height of 3.90 m. We employ a structured mesh with $\delta = 0.01\sqrt{2}$ m, and time step is $1.2 \cdot 10^{-5}$ s; hydrodynamics solution parameter $\Upsilon = \Delta l/(12000\varepsilon)$ to capture properly when entrapped air is explosively released to the atmosphere. Remaining parameters are the same as previous test.

Water starts to emerge from the duct at $t = 0.51$ s, when air cavity head is situated at a height of 0.8 m. Selected results at subsequent times are shown in Fig. 27. Fig. 27(a) depicts the water phase at time 1.38 s. At this time, air cavity head is still traveling inside the duct and free surface has a twofold shape. Along with the radial propagation of a shallow layer of water, a volume of water with mushroom shape is raising, in agreement with observations (see Fig. 27(b), captured from a real footage in https://www.youtube.com/watch?v=dM2L9EHNM5o). When air bubble head reaches ground level, water and air are expelled upwards in the form of a high velocity jet (see Fig. 27(e)). Fig. 27(d) shows a slice of the numerical results, highlighting the mixing of phases (blue signifies $\phi = 1$ and white corresponds to $\phi = 0$). Although the model does not cover all the subtle details of the highly complex mixing, it achieves a good agreement with the general topology of the phenomenon. The distribution shows, both in real case and in numerical case, a shallow radial flux, two central widening of the jet, and a sharp front propagating in vertical direction.

The foregoing experiment was repeated with the full three dimensional capability in action to evaluate the adequacy of the axisymmetric assumption. The unstructured tetrahedral mesh has 2610436 nodes, $\Delta t = 5 \cdot 10^{-5}$ s, and $\Upsilon = \Delta l/(6\varepsilon)$. Figs. 27(c) and 27(f) illustrate the geyser at $t = 1.440$ s and at $t = 1.848$ s, respectively. Air bubble reaches the top of the duct at $t = 1.554$ s, while in axisymmetric solution this time is 1.434 s. This lag is ascribed to the small overprediction of the bubble velocity by the axisymmetric model when bubble's head is close to the free surface (this trend can be observed in Fig. 26(b)). Besides, there is not enough resolution of the three
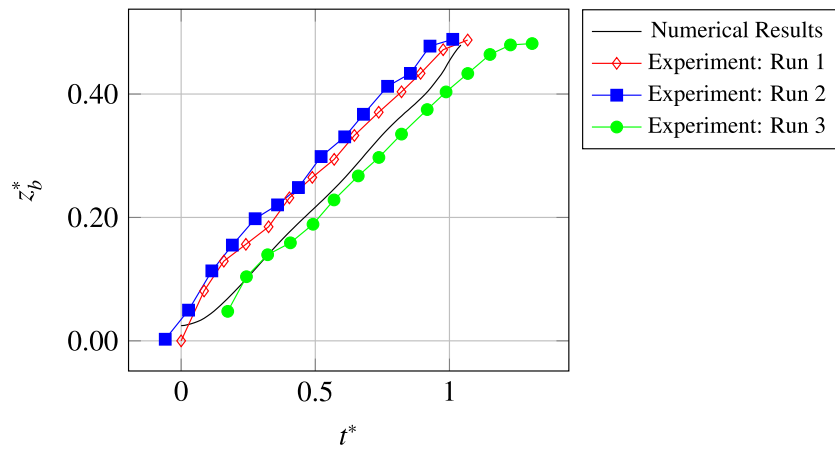
(a) Bubble position
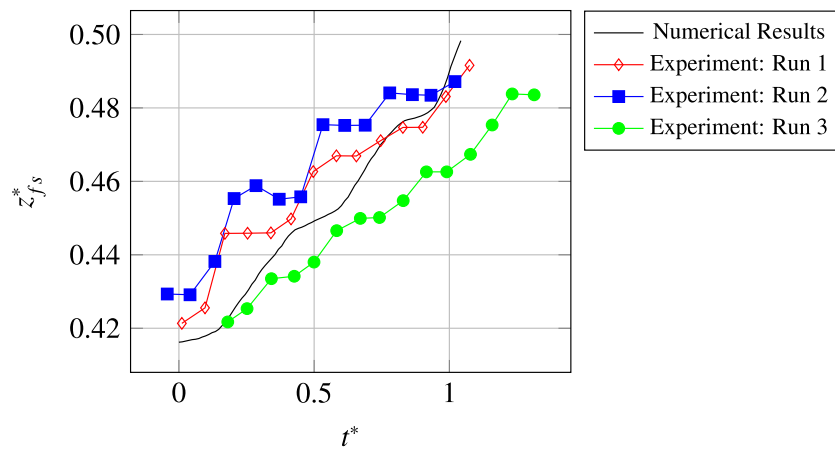
(b) Free surface position
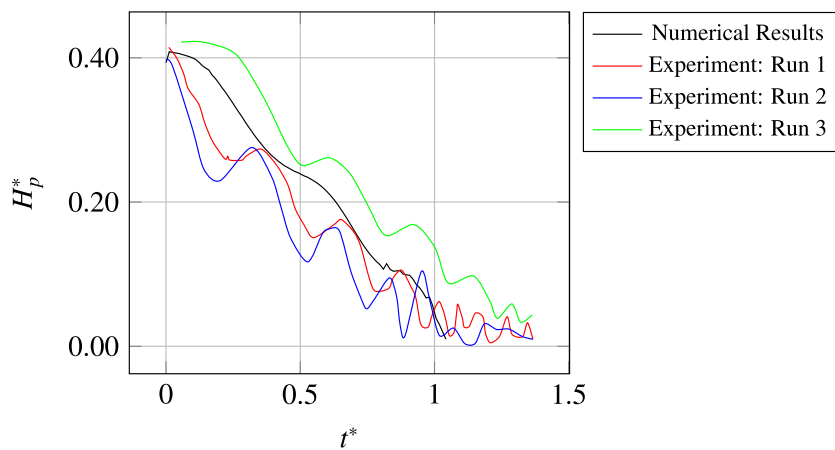
(c) Bubble Pressure

Fig. 26. Taylor bubble emergence. Comparison between axisymmetric model and experimental results [4]. (For interpretation of the references to color in this figure legend, the reader is referred to the web version of this article.)
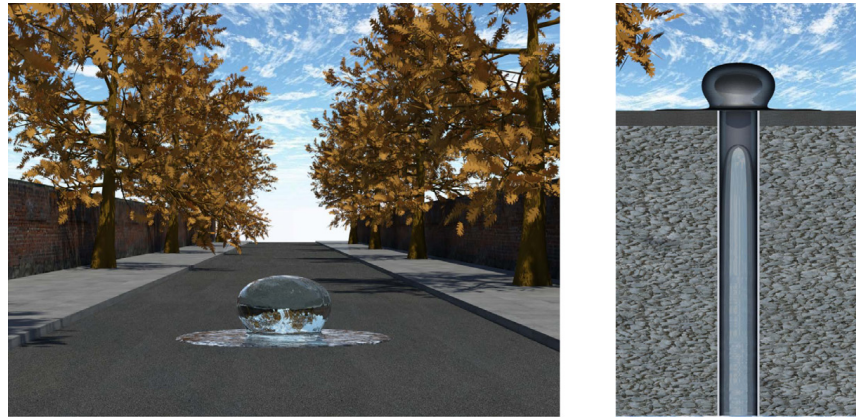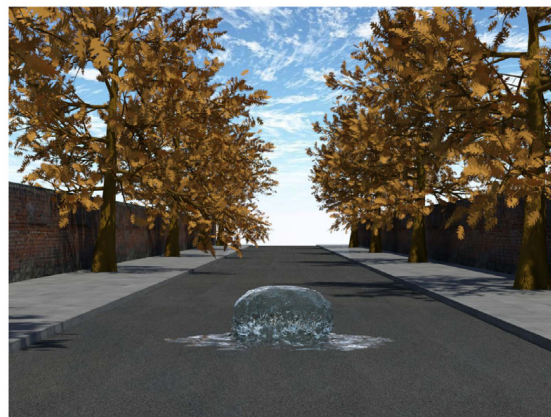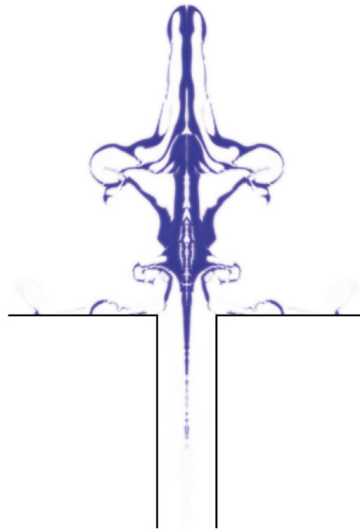
(a) Axisymmetric numerical results at t=1.380 s

(b) Frame from a footage of a geyser (https://www.youtube.com/watch?v=dM2L9EHNM5o)

(c) Three dimensional numerical results at t=1.440 s

Fig. 27. Geysering simulation. (For interpretation of the references to color in this figure legend, the reader is referred to the web version of this article.)

dimensional mesh to capture details of the thin water layers attached to the vertical duct wall. Hence an artificial water/air mixing slows down at some extent the bubble ascension. Overall, flow pattern is almost axisymmetric and full 3D model results are very similar to results obtained with the simplified model until bubble head reaches street

(d) Slice for axisymmetric numerical results at *t*=1.578 s

(e) Frame from a footage of a geyser (2) (https://www.youtube.com/watch?v=dM2L9EHNM5o)

(f) Three dimensional numerical results at *t*=1.848 s

Fig. 27. (*continued*).

level (see Fig. 27(c)). Once water and air are expelled from the duct, three dimensional simulation differs from axisymmetric, yet main topological features remain very similar (see Fig. 27(f)).

4. Final remarks

The weakly compressible flow model proposed succeeds in the approach to challenging interface fluid dynamics that requires, recurrently, a precise capture of the interface topology as well as an instantaneous adaptation to ever-changing conditions. A paradigm of these flows is the genesis and propagation of air cavities in conduits, combining virtually-potential well-defined interfaces with diffuse regions having complex momentum exchange between air and water. A relevant portion of numerical experiments has scrutinized the three stages of air cavity occurrence. Results revealed that, although air pressure increase is small, expansion/compression of the bubble makes weak-compressibility assumption necessary for an appropriate momentum transfer between fluids. Three dimensional simulations (or, at least, axisymmetrical for circular conduits) are demanded for proper answers when air pressure reaches the levels mentioned above, particularly for heavily accelerated air pockets, as is the case of vertical ducts. Deficiencies in two-dimensional outputs are apparent in bubble celerity, air pressure, and in the water free surface coupling with cavity motion.

Parametrical definition of density for weakly compressible fluids can be consequential for conservation. To recover mass conservation present in the incompressible limit, continuity equation has been modified in the split numerical approach. Besides, parametrical definition of density gives rise to a virtual stratification between phases. To attend to the precise capture of interface, the current decrease of transition length produces very unstable high density gradient transitions. In this situation, stability analysis establishes the beneficial effect of an active equivalent surface tension force to attenuate high frequency wiggles. To reduce band thickness, while preserving original density interpolation, we present an adaptive mesh refinement in the interface neighborhood. Conservation and monotonicity of variables are stated in refinement/unrefinement processes by means of an algorithm based on flux correction technique. Refinement is performed by nested grids, enabling undemanding dynamic computation.

Surface capturing by advecting a phase function in a VOF manner involves the well-known numerical drawbacks of advecting a (nearly) discontinuous phase distribution. The fully conservative and sign-preserving finite element transport algorithm developed has added cost-effective features to accomplish sharp interface solutions with low enclosed volume and interface errors. Reinitialization step complements the transport algorithm via a non-linear anisotropic diffusion equation streamlined in the normal direction of the interface. Equation is solved by a fast-converging iterative procedure incorporating a simple diffusive flux correction. Accuracy of interface capture is powered by constraining interface normal calculation to few elements surrounding it, and by extending normal values from nearest element containing interface. Although this restriction is inexpensive and reduces interface errors, it is less effective when the flow has very close multiple contact discontinuities. More advanced processes for normal computation depending on the local dynamics is the feasible solution in this situation; this issue will be pursued in future work. However, extensive three-dimensional numerical testing showed that the use of more elaborated normal calculations, and/or the covering of large areas far from the interface, have a severe charge on computational time.

In addition to an efficient interface capturing procedure, flow algorithm must detect the presence of the transition during correction, to be capable of controlling artificial momentum jumps across the interface. This goal is reached by preventing formation of new limits across the interface with an adequate local choice of bounds for flux correction. The enhanced limiting process is very convenient for flows with very low density ratio, and, particularly, for problems with highly oscillating free surface, such as low (supercritical) Froude number flows.

Complete coupled simulation of air cavities stages is of interest to survey real sewer lay-outs where cavity genesis and geysering occurs. Moreover, the coupling of the present model with shallow water flow models to simulate street level surface flows is an encouraging issue for integrated studies of urban floodings. These and related topics exceed the scope of the present work, and will be developed in the future.

Acknowledgments

Appendix A. Stability of artificial stratified flow

To examine stability of two phase flow with a diffused interface we consider an initial state of an incompressible inviscid flow with density and velocity distributions given by Eqs. (25) and (26), respectively. These distributions are repeated for clarity,

$$
\rho(y) = \begin{cases} \rho_1 + \frac{\rho_2 - \rho_1}{2} e^{-y/L_\rho} & if \quad y > 0 \\[2mm] \rho_2 + \frac{\rho_1 - \rho_2}{2} e^{y/L_\rho} & if \quad y < 0 \end{cases},
$$

$$
u(y) = \begin{cases} u_1 + \frac{u_2 - u_1}{2} e^{-y/L_u} & if \quad y > 0 \\[2mm] u_2 + \frac{u_1 - u_2}{2} e^{y/L_u} & if \quad y < 0 \end{cases},
$$

where L_ρ, L_u are parameters that control density and velocity gradients. We introduce the coordinate value y_b to indicate the position of a density iso-surface, thus $\rho(y = y_b(x, t))$ is constant. Then, by designating as $\tilde{\rho}$, $\tilde{u}$, $\tilde{v}$, $\tilde{p}$, and $\tilde{y}_b$ the perturbed density, x and y velocity components, pressure, and density iso-surface position, respectively, the two-dimensional linearized equations governing the perturbation field can be written, following Ref. [27], as

$$
\frac{\partial \tilde{\rho}}{\partial t} + u \frac{\partial \tilde{\rho}}{\partial x} = -\tilde{v} \frac{\partial \rho}{\partial y}, \tag{35}
$$

$$
\frac{\partial \tilde{u}}{\partial x} + \frac{\partial \tilde{v}}{\partial y} = 0, \tag{36}
$$

$$
\rho \frac{\partial \tilde{u}}{\partial t} + \rho u \frac{\partial \tilde{u}}{\partial x} + \rho \tilde{v} \frac{\partial u}{\partial y} = -\frac{\partial \tilde{p}}{\partial x}, \tag{37}
$$

$$
\rho \frac{\partial \tilde{v}}{\partial t} + \rho u \frac{\partial \tilde{v}}{\partial x} = -\frac{\partial \tilde{p}}{\partial y} - g\tilde{\rho} + \sigma \frac{\partial^2 \tilde{y}_b}{\partial x^2} \left[\left(\frac{\partial \rho}{\partial y} \frac{1}{\rho_1 - \rho_2} \right) \frac{2\rho}{\rho_1 + \rho_2} \right]_{y=y_b}, \tag{38}
$$

$$
\frac{\partial \tilde{y}_b}{\partial t} + u_b \frac{\partial \tilde{y}_b}{\partial x} = \tilde{v}_b. \tag{39}
$$

Eq. (35) is the mass conservation of the perturbed field, Eq. (36) is the solenoidal condition for the perturbed velocity field, Eqs. (37) and (38) are the momentum equations for x and y components, respectively, and Eq. (39) is the kinematic condition applied at a density iso-surface $y = y_b$. Variables with subscript b are evaluated at $y = y_b$ and σ is the surface tension coefficient value. Eq. (38) includes the equivalent surface tension force of the continuous model (10).

To seek solutions of the form $\exp(iKx + st)$, where $\text{Re}(s)$ is the growth rate, and K is the perturbation wave number, Eqs. (35)–(39) become, after replacement,

$$
(s + iKu)\tilde{\rho} = -\tilde{v} \frac{\partial \rho}{\partial y}, \tag{40}
$$

$$
iK\tilde{u} = -\frac{\partial \tilde{v}}{\partial y}, \tag{41}
$$

$$
\rho(s + iKu)\tilde{u} + \rho\tilde{v} \frac{\partial u}{\partial y} = -iK\tilde{p}, \tag{42}
$$

$$
\rho(s + iKu)\tilde{v} = -\frac{\partial \tilde{p}}{\partial y} - g\tilde{\rho} - K^2\sigma \tilde{y}_b \left[\left(\frac{\partial \rho}{\partial y} \frac{1}{\rho_1 - \rho_2} \right) \frac{2\rho}{\rho_1 + \rho_2} \right]_{y=y_b}, \tag{43}
$$

$$
(s + iKu)\tilde{y}_b = \tilde{v}_b. \tag{44}
$$

Now, we eliminate $\tilde{u}$ in Eq. (42) by means of Eq. (41), and eliminate $\tilde{\rho}$ and $\tilde{y}_b$ in Eq. (43) by means of Eqs. (40) and (44). The resulting equations are

$$
-\rho(s + iKu)\frac{\partial \tilde{v}}{\partial y} + iK\rho\tilde{v} \frac{\partial u}{\partial y} = K^2 \tilde{p}. \tag{45}
$$

$$
\rho(s + iKu)\tilde{v} = -\frac{\partial \tilde{p}}{\partial y} + g\tilde{v} \frac{\partial \rho}{\partial y} \frac{1}{s + iKu} - K^2\sigma \frac{\tilde{v}}{s + iKu} \left(\frac{\partial \rho}{\partial y} \frac{1}{\rho_1 - \rho_2} \right) \frac{2\rho}{\rho_1 + \rho_2}. \tag{46}
$$

Finally, by inserting Eq. (45) into Eq. (46), an equation dependent on vertical perturbed velocity is attained,

$$\frac{\partial}{\partial y}\left[-\rho(s+iKu)\frac{\partial \tilde{v}}{\partial y} + iK\tilde{v}\rho\frac{\partial u}{\partial y}\right] + K^2\rho(s+iKu)\tilde{v} -$$

$$gK^2\tilde{v}\frac{\partial \rho}{\partial y}\frac{1}{(s+iKu)} + K^4\sigma\frac{\tilde{v}}{s+iKu}\left(\frac{\partial \rho}{\partial y}\frac{1}{\rho_1-\rho_2}\right)\frac{2\rho}{\rho_1+\rho_2} = 0. \tag{47}$$

Integration along vertical direction of Eq. (47) in the domain $(-\infty, \infty)$ can be written as

$$\int_{-\infty}^{\infty}\left((s+iKu)(K^2\rho\tilde{v}) - \frac{K^2g}{s+iKu}\frac{\partial \rho}{\partial y}\tilde{v} + K^4\sigma\frac{\tilde{v}}{s+iKu}\left(\frac{\partial \rho}{\partial y}\frac{1}{\rho_1-\rho_2}\right)\frac{2\rho}{\rho_1+\rho_2}\right)dy = 0, \tag{48}$$

noting that integration of first term in Eq. (47) is null. By assuming $L_\rho = L_u = L_I$, integration results in

$$-s^2K(\rho_1+\rho_2) - \frac{iK^2s}{(1+KL_I)(2+KL_I)}((4+KL_I(3+KL_I))\rho_1 u_1 +$$

$$KL_I(3+KL_I)\rho_1 u_2 + \rho_2(4u_2 + KL_I(3+KL_I)(u_1+u_2)))+$$

$$\frac{K}{4(1+KL_I)(2+KL_I)}(4gK(2+KL_I)(\rho_1-\rho_2)+$$

$$K^2(8\rho_1 u_1^2 + 8\rho_2 u_2^2 + K^2L_I(-4\sigma + L_I(\rho_1+\rho_2)(u_1+u_2)^2)+$$

$$K(-8\sigma + 3L_I(\rho_1+\rho_2)(u_1+u_2)^2))) = 0. \tag{49}$$

In case of $L_I = 0$ in Eq. (49), and $\mathrm{Re}(s) = 0$, stability condition for non-stratified two fluids problem (24) is recovered.

Now, consider a transition band thin enough such that, although interface is diffuse, approximation could assume an interface at $y = y_b = 0$. At $y = 0$ surface tension brings into play. In this case Eq. (48) turns into

$$\int_{-\infty}^{\infty}\left((s+iKu)(K^2\rho\tilde{v}) - \frac{K^2g}{s+iKu}\frac{\partial \rho}{\partial y}\tilde{v} + K^4\sigma\frac{\tilde{v}}{s+iKu}\delta_d(y)\right)dy = 0, \tag{50}$$

since $\lim_{L_I\to 0}\left(\frac{\partial \rho}{\partial y}\frac{1}{\rho_1-\rho_2}\right) = \delta_d(y)$, and $2\rho(y=0)/(\rho_1+\rho_2) = 1$, where δ_d is the Dirac-delta function. Integration of Eq. (50) yields to

$$-s^2K(\rho_1+\rho_2) - \frac{iK^2s}{(1+KL_I)(2+KL_I)}((4+KL_I(3+KL_I))\rho_1 u_1 +$$

$$KL_I(3+KL_I)\rho_1 u_2 + \rho_2(4u_2 + KL_I(3+KL_I)(u_1+u_2)))+$$

$$\frac{K}{4(1+KL_I)(2+KL_I)}(4gK(2+KL_I)(\rho_1-\rho_2)+$$

$$K^2(-4K^3L_I^2\sigma + 8\rho_1 u_1^2 + 8\rho_2 u_2^2 +$$

$$K^2L_I(-12\sigma + L_I(\rho_1+\rho_2)(u_1+u_2)^2)+$$

$$K(-8\sigma + 3L_I(\rho_1+\rho_2)(u_1+u_2)^2))) = 0. \tag{51}$$

Appendix B. Error estimation for a general density interpolation

A mass error estimation is derived for the modified density interpolation

$$\rho(\phi) = \begin{cases} \rho_1 & if & \phi < 1/2 - \vartheta \\ \rho_1 + (\phi - 1/2 + \vartheta)\frac{\rho_2-\rho_1}{2\vartheta} & if & 1/2 - \vartheta \le \phi \le 1/2 + \vartheta \\ \rho_2 & if & \phi > 1/2 + \vartheta. \end{cases}$$

To perform integration we consider the domain $\Omega = \Omega_1 \cup \Omega_2 \cup \Omega_3$, where $\{\phi = 0\} \cup \{\phi = 1\}$ in Ω_1, $\phi \in [0, 1/2 - \vartheta] \cup [1/2 + \vartheta, 1]$ in Ω_2, and $\phi \in [1/2 - \vartheta, 1/2 + \vartheta]$ in Ω_3. Mass error at time t^n is calculated by subtracting from the density function the original linear density interpolation with zero mass error, $\rho(\phi) = \rho_1(1 - \phi) + \rho_2\phi$. Thus,

$$e(M) = \int_{\Omega_1 + \Omega_2 + \Omega_3} [\rho - \rho_1(1 - \phi) - \rho_2\phi] \, d\Omega \ .$$

Integrals for each subdomain are

$$\mathcal{I}_1 = \int_{\Omega_1} [\rho - \rho_1(1 - \phi) - \rho_2\phi] \, d\Omega_1 = 0 \ ,$$

$$\mathcal{I}_2 = \int_{\Omega_2} [\rho - \rho_1(1 - \phi) - \rho_2\phi] \, d\Omega_2 = (\rho_1 - \rho_2) \int_{\Omega_{2a}} \phi \, d\Omega_{2a} + (\rho_2 - \rho_1) \int_{\Omega_{2b}} (1 - \phi) \, d\Omega_{2b} \ ,$$

$$\mathcal{I}_3 = \int_{\Omega_3} \left[\rho_1 + (\phi - 1/2 + \vartheta)\frac{\rho_2 - \rho_1}{2\vartheta} - \rho_1(1 - \phi) - \rho_2\phi \right] d\Omega_3 = \frac{\rho_2 - \rho_1}{4\vartheta} \int_{\Omega_3} (2 - 4\vartheta)(\phi - 1/2) \, d\Omega_3 \ ,$$

where Ω_{2a} and Ω_{2b} are sub-spaces of Ω_2 such that $\phi \in [0, 1/2 - \vartheta]$ in Ω_{2a} and $\phi \in [1/2 + \vartheta, 1]$ in Ω_{2b}.

Now we assume a straight interface with length L_Γ, and an exponential phase function [12], $\phi(n) = \dfrac{1}{1 + e^{-n/\varepsilon}}$, where n is the interface normal. Then,

$$\mathcal{I}_2 = -L_\Gamma(\rho_2 - \rho_1) \int_{-\infty}^{\varepsilon \log\left(\frac{1/2 - \vartheta}{1/2 + \vartheta}\right)} \phi(n) \, dn + L_\Gamma(\rho_2 - \rho_1) \int_{\varepsilon \log\left(\frac{1/2 + \vartheta}{1/2 - \vartheta}\right)}^{\infty} [1 - \phi(n)] \, dn \ ,$$

$$\mathcal{I}_3 = L_\Gamma \frac{\rho_2 - \rho_1}{4\vartheta} \int_{\varepsilon \log\left(\frac{1/2 - \vartheta}{1/2 + \vartheta}\right)}^{\varepsilon \log\left(\frac{1/2 + \vartheta}{1/2 - \vartheta}\right)} (2 - 4\vartheta)(\phi(n) - 1/2) \, dn \ .$$

Although $\mathcal{I}_1 + \mathcal{I}_2 + \mathcal{I}_3 = 0$ because analytical phase function is symmetrical with respect to $\phi = 1/2$, numerical results are not symmetrical. A mass error bound is established by computing integrals only for interval $n \in (0, \infty)$. Now,

$$\mathcal{I}_1 + \mathcal{I}_2 + \mathcal{I}_3 = L_\Gamma \frac{\rho_2 - \rho_1}{4\vartheta} \int_0^{\varepsilon \log\left(\frac{1/2 + \vartheta}{1/2 - \vartheta}\right)} (2 - 4\vartheta)(\phi(n) - 1/2) \, dn + L_\Gamma(\rho_2 - \rho_1) \int_{\varepsilon \log\left(\frac{1/2 + \vartheta}{1/2 - \vartheta}\right)}^{\infty} [1 - \phi(n)] \, dn \ ,$$

resulting in the error bound

$$|e(M)| < \left| L_\Gamma(\rho_2 - \rho_1)\varepsilon \left(\log\left(\frac{2}{1 + 2\vartheta}\right) + \frac{2\vartheta - 1}{4\vartheta} \log((1 + 2\vartheta)(1 - 2\vartheta)) \right) \right| \ . \tag{52}$$

References

[1] T.B. Benjamin, Gravity currents and related phenomena, J. Fluid Mech. 31 (02) (1968) 209–248.

[2] D.L. Wilkinson, Motion of air cavities in long horizontal ducts, J. Fluid Mech. 118 (1982) 109–122.

[3] W.D. Baines, Air cavities as gravity currents on slope, J. Hydraul. Eng. ASCE 117 (1992) 1600–1615.

[4] J.G. Vasconcelos, S.J. Wright, Geysering generated by large air pockets released through water-filled ventilation shafts, J. Hydraul. Eng. 137 (2011) 543–555.

[5] H. Bashiri-Atrabi, T. Hosoda, Assessment of two-equation model for simulation of air pocket advancing into a rectangular duct, J. Hydraul. Res. 57 (2019) 122–130.

[6] R. Löhner, C. Yang, E. Oñate, On the simulation of flows with violent free surface motion, Comput. Methods Appl. Mech. Engrg. 195 (2006) 5597–5620.

[7] C. Hirt, B. Nichols, Volume of fluid (VOF) method for the dynamics of free boundaries, J. Comput. Phys. 39 (1981) 201–225.

[8] S. Osher, J.A. Sethian, Fronts propagating with curvature-dependent speed: Algorithms based on Hamilton–Jacobi formulations, J. Comput. Phys. 79 (1988) 12–49.

[9] M. Cruchaga, L. Battaglia, M. Storti, J. D'Elía, Numerical modeling and experimental validation of free surface flow problems, Arch. Comput. Methods Eng. 23 (2016) 139–169.

[10] F. Gibou, D. Hyde, R. Fedkiw, Sharp interface approaches and deep learning techniques for multiphase flows, J. Comput. Phys. 380 (2019) 442–463.

[11] E. Olsson, G. Kreiss, A conservative level set method for two phase flow, J. Comput. Phys. 210 (2005) 225–246.

[12] E. Olsson, G. Kreiss, S. Zahedi, A conservative level set method for two phase flow II, J. Comput. Phys. 225 (2007) 785–807.

[13] L. Zhao, J. Mao, X. Bai, X. Liu, T. Li, J. Williams, Finite element implementation of an improved conservative level set method for two-phase flow, Comput. & Fluids 100 (2014) 138–154.

[14] R. Chiodi, O. Desjardins, A reformulation of the conservative level set reinitialization equation for accurate and robust simulation of complex multiphase flows, J. Comput. Phys. 343 (2017) 186–200.

[15] M. Quezada, D. Kuzmin, C.E. Kees, A monolithic conservative level set method with built–in redistancing, J. Comput. Phys. 379 (2019) 262–278.

[16] P. Ortiz, Non-oscillatory continuous fem for transport and shallow water flows, Comput. Methods Appl. Mech. Engrg. 223–224 (2012) 55–69.

[17] J.P. Boris, D.L. Book, Flux-corrected transport. I. SHASTA, a fluid transport algorithm that works, J. Comput. Phys. 11 (1973) 38–69.

[18] R. Löhner, K. Morgan, J. Peraire, M. Vahdati, Finite element flux-corrected transport (FEM–FCT) for the Euler and Navier–Stokes equations, Internat. J. Numer. Methods Fluids 7 (1987) 1093–1109.

[19] S.T. Zalesak, The design of flux–corrected transport (FCT) algorithms on structured grids (Ph.D. thesis), George Mason University (USA), 2005.

[20] P. Ortiz, A positive definite continuous FEM model for advection, Adv. Water Resour. 32 (2009) 1359–1371.

[21] A. Harten, The artificial compression method for computation of shocks and contact discontinuities: I. Single conservation laws, Comm. Pure Appl. Math. 30 (1977) 611–638.

[22] J.-L. Guermond, M.Q. de Luna, T. Thompson, A conservative anti-diffusion technique for the level set method, J. Comput. Appl. Math. 321 (2017) 448–468.

[23] J. Molina, P. Ortiz, A conservative flux–corrected continuous FEM for fluid interface dynamics, Internat. J. Numer. Methods Fluids 91 (2019) 287–310.

[24] O. Zienkiewicz, P. Nithiarasu, R. Codina, M. Vázquez, P. Ortiz, The characteristic-based-split procedure: An efficient and accurate algorithm for fluid problems, Internat. J. Numer. Methods Fluids 31 (1999) 359–392.

[25] P. Ortiz, O. Zienkiewicz, J. Szmelter, Hydrodynamics and transport in estuaries and rivers by the CBS finite element method, Internat. J. Numer. Methods Engrg. 66 (2006) 1569–1586.

[26] O. Zienkiewicz, R. Taylor, P. Nithiarasu (Eds.), The Finite Element Method for Fluid Dynamics, seventh ed., Butterworth-Heinemann, Oxford, 2014.

[27] S. Chandrasekhar, Hydrodynamic and hydromagnetic stability, in: Dover Books on Physics Series, Dover Publications, 1961.

[28] J.D. Ramshaw, J.A. Trapp, Characteristics, stability, and short wavelength phenomena in two–phase flow equation systems, Nucl. Sci. Eng. 66 (1978) 93–102.

[29] G.V. Miloshevsky, A. Hassanein, Modelling of Kelvin–Helmholtz instability and splashing of melt layers from plasma–facing components in tokamaks under plasma impact, Nucl. Fusion 50 (2010) 115005.

[30] J.U. Brackbill, D.B. Kothe, C. Zemach, A continuum method for modeling surface tension, J. Comput. Phys. 100 (1992) 335–354.

[31] R.J. LeVeque, High-resolution conservative algorithms for advection in incompressible flow, SIAM J. Numer. Anal. 33 (1996) 627–665.

[32] K.M.T. Kleefsman, G. Fekken, A.E.P. Veldman, B. Iwanowski, B. Buchner, A volume-of-fluid based simulation method for wave impact problems, J. Comput. Phys. 206 (2005) 363–393.

[33] S.T. Zalesak, Fully multidimensional flux-corrected transport algorithms for fluids, J. Comput. Phys. 31 (1979) 335–362.

[34] D. Kuzmin, M. Möller, Algebraic flux correction II: Compressible Euler equations, in: D. Kuzmin, R. Löhner, S. Turek (Eds.), Flux Corrected Transport: Principles, Algorithms and Applications, Springer, 2005, pp. 208–251.

[35] K. Mikaelian, Approximate treatment of density gradients in Rayleigh–Taylor instabilities, Phys. Rev. A 33 (1986) 1216–1222.

[36] L.F. Wang, C. Xue, W.H. Ye, Y.J. Li, Destabilizing effect of density gradient on the Kelvin–Helmholtz instability, Phys. Plasmas 16 (2009) 112104.

[37] H. Nguyen, J.-R.C. Cheng, C.R. Berger, G. Savant, A mass conservation algorithm for adaptive unrefinement meshes used by finite element methods, Procedia Comput. Sci. 9 (2012) 727–736.

[38] J.R. Cebral, R. Lohner, Conservative load projection and tracking for fluid–structure problems, AIAA J. 35 (1997) 687–692.

[39] H. Kim, M.-S. Liou, Accurate adaptive level set method and sharpening technique for three dimensional deforming interfaces, Comput. & Fluids 44 (2011) 111–129.

[40] C. Kees, I. Akkerman, M. Farthing, Y. Bazilevs, A conservative level set method suitable for variable-order approximations and unstructured meshes, J. Comput. Phys. 230 (2011) 4536–4558.

[41] P. Ortiz, Shallow water flows over flooding areas by a flux–corrected finite element method, J. Hydraul. Res. 52 (2014) 241–252.

[42] R.M. Davies, G.I. Taylor, The mechanics of large bubbles rising through extended liquids and through liquids in tubes, Proc. R. Soc. Lond. Ser. A Math. Phys. Eng. Sci. 200 (1950) 375–390.

[43] P.R. Garabedian, On steady-state bubbles generated by taylor instability, Proc. R. Soc. Lond. Ser. A Math. Phys. Eng. Sci. 241 (1957) 423–431.

[44] P.K. Kundu, I.M. Cohen, D.R. Dowling, Fluid Mechanics, fifth ed., Academic Press, Boston, 2012.

[45] Paraview, open source visualization, 2014, http://www.paraview.org.

[46] Autodesk 3ds max, 2016, https://www.autodesk.com/products/3ds-max/overview.